Microwave spectroscopy of the high-L H_2 Rydberg states ($v=0$, $R=1$) $n=10$ G, H, I, and K

W. G. Sturrus,* E. A. Hessels, P. W. Arcuni,[†] and S. R. Lundeen

Department of Physics, University of Notre Dame, Notre Dame, Indiana 46556

(Received 16 October 1990; revised manuscript received 29 April 1991)

Ten fine-structure intervals separating $n=10$, $L=4$, 5, 6, and 7 Rydberg states of H_2, all with ($v=0$, $R=1$) H_2^+ cores, have been measured using fast-beam microwave-optical techniques, determining the relative positions of all these states to a precision of about ± 0.3 MHz. These experimental results are compared with predictions of the expected structure, which use the polarization model to relate the Rydberg fine structure to properties of the H_2^+ ion, yielding experimental determinations of certain electric properties of the (0,1) state of H_2^+: quadrupole moment, $Q=1.642\,95(30)ea_0^2$, and dipole polarizabilities, $\alpha_S=3.1770(34)a_0^3$, $\alpha_T=4.015(36)a_0^3$.

I. INTRODUCTION

The high-L Rydberg states of H_2 are characterized by one excited electron in a nonpenetrating, nearly hydrogenic orbit, bound by the net charge of the nearly free H_2^+ ion core. Because the coupling between the two parts of the system is so weak, and because both parts of the system can be described precisely in isolation, it is possible to calculate the properties of these states to much higher precision than would be possible in an arbitrary state of the H_2 molecule. This provides a special motivation for studying the spectroscopy of these states with high experimental precision.

Since the zeroth-order picture of these states in terms of a free H_2^+ ion and a hydrogenic electron is so nearly exact, many properties of the H_2^+ ion, such as dipole polarizabilities, electric quadrupole moment, and hyperfine constants, are reflected in the fine structure of high-L Rydberg states. Indeed, in many ways the Rydberg electron is an ideal probe to explore these properties. The H_2^+ ion, the simplest molecule, plays a fundamental role in molecular science, and many of its properties have been carefully calculated. There are, however, rather few precise experimental measurements with which these calculations can be compared [1]. The available precise measurements fall into three classes. The earliest were the determination of hyperfine-structure constants of H_2^+ in vibrationally excited states ($v=4,5,6,7,8$), which were carried out by Jefferts using an ion-trap technique [2]. These measurements were partially motivated by the (so far unsuccessful) hope of detecting interstellar H_2^+ by observing the characteristic radio-frequency emissions from its ground-state hyperfine structure. A number of theoretical calculations have predicted (or explained) the observed hyperfine constants with a fair degree of success, although a systematic discrepancy of about one part

in 10^4 in the dominant dipole hyperfine constant has only recently been explained [3]. A second line of precise measurements is the study by infrared laser spectroscopy of rotational-vibrational transitions in HD^+, initially carried out by Wing and collaborators in low vibrational states [4], and later extended to much higher vibrational states by Carrington, Mcnab, and Montgomerie [5]. These measurements have stimulated considerable improvements in theoretical predictions of the rotational-vibrational structure of HD^+ and H_2^+, which are now close to the level of experimental precision [6,7]. A third independent line of precision measurement is the recent measurement of the g value of the H_2^+ ground electronic state using an ion-trap technique [8], which gives a result in agreement with theoretical predictions [9]. These existing measurements by no means exhaust the list of measurable properties of the H_2^+ ground electronic state. Indirect measurements of such properties, obtained by study of the spectroscopy of high-L H_2 Rydberg levels, could lead to substantial new information about this fundamental system.

The theoretical description of the high-L H_2 states in terms of properties of the free H_2^+ ion has been obtained using a polarization model formulation [10,11], quite similar to that used by Drachman [12] to describe high-L states of the helium atom. This is an approach to calculating the eigenvalues of the Coulomb Hamiltonian subject to the two basic assumptions (1) the two electrons are treated as distinguishable particles, and (2) penetration of the core by the Rydberg electron is neglected. This formulation expresses the interactions between the Rydberg electron and the ion core (beyond the dominant Coulomb interaction) in terms of an effective potential, the "polarization potential" V_{pol}, which includes the effects of both permanent and induced multipole moments of the core. The lowest few terms of a systematic multipole expansion of this effective potential are

$$V_{\text{pol}} = -\frac{e\,Q(\rho)}{r^3}P_2(\cos\theta) - \frac{e^2}{r^4}\left[\frac{\alpha_S(\rho)}{2} + \frac{\alpha_T(\rho)}{3}P_2(\cos\theta)\right] - \frac{e\,\phi(\rho)}{r^5}P_4(\cos\theta)$$

$$- \frac{e^2}{r^6}\left[\frac{C_0(\rho)}{10} + \frac{C_1(\rho)}{7}P_2(\cos\theta) + \frac{12C_2(\rho)}{35}P_4(\cos\theta)\right] + \frac{e^4 a_0}{r^6}[\tfrac{3}{2}\beta_S(\rho) + \tfrac{1}{2}\beta_T(\rho)P_2(\cos\theta)]$$

$$- \frac{e^2}{r^6}\left[\frac{E_1(\rho)}{7}P_2(\cos\theta) + \frac{E_2(\rho)}{35}P_4(\cos\theta)\right], \tag{1}$$

where r is the radial coordinate of the Rydberg electron and θ is the polar angle of that electron's position with respect to the internuclear axis. The coefficients that occur in V_{pol} are Q, the electric quadrupole moment; α_S and α_T, the scalar and tensor adiabatic dipole polarizabilities; ϕ, the electric hexadecapole moment; C_0, C_1, and C_2, the scalar and tensor adiabatic quadrupole polarizabilities; β_S and β_T, the scalar and tensor nonadiabatic dipole polarizabilities; and E_1, and E_2, the tensor adiabatic dipole-octupole polarizabilities. These coefficients are all properties of the free H$_2^+$ ion, which in general depend on the internuclear separation ρ, and hence will have a different average for each rotational-vibrational state. All of these constants have been calculated [13].

The zeroth-order basis appropriate to the high-L Rydberg states is a set of vector-coupled product states characterized by (v,R), the vibrational and rotational quantum numbers of the H$_2^+$ core; (n,L), the principal quantum number and orbital angular momentum of the Rydberg electron; and $\mathbf{N} = \mathbf{R} + \mathbf{L}$, the vector sum of core angular momentum $\mathbf{R}$ and Rydberg electron angular momentum $\mathbf{L}$. We refer to such states using the notation $(v,R)nL_N$, and the energy of this zeroth-order state as $E^{[0]}((v,R)nL_N)$. The expectation value of V_{pol} for such a basis state accounts for the major part of the nonhydrogenic structure,

$$E_{\text{pol}}^{[1]} = \langle \varphi_0 | V_{\text{pol}} | \varphi_0 \rangle . \tag{2}$$

We refer to $E_{\text{pol}}^{[1]}$ as a state's "first-order polarization energy." It can also be shown that V_{pol} can approximately account for the mixing of different Rydberg basis functions by long-range interactions with the H$_2^+$ core [11]. This produces a contribution to the energy of each Rydberg level that is formally identical to the expression for the "second-order polarization energy" in a simple perturbation scheme,

$$E_{\text{pol}}^{[2]} = \sum_j \frac{|\langle \varphi_0 | V_{\text{pol}} | \varphi_j \rangle|^2}{E_0 - E_j}, \tag{3}$$

where φ_j is any other Rydberg state. The total energy of any particular Rydberg level may be estimated as the sum of its zeroth-order energy and the fine-structure energy, which is the sum of Eqs. (2) and (3). We call this fine structure electric fine structure (EFS), since it is due only to electric interactions, neglecting all spins. Clearly, since such a calculation depends parametrically on the H$_2^+$ properties listed above, which occur as coefficients in the polarization potential V_{pol}, its accuracy is limited by the precision with which these coefficients are known. However, quite independently, its accuracy may also be limited by the truncation of the perturbation theory which the polarization model represents. For example, the polarization potential [Eq. (1)] omits terms proportional to higher inverse powers of r than r^{-6}, and this would certainly be expected to limit the accuracy of the results at some level. In the closely analogous calculation of helium fine structure by Drachman [12], this truncation is the primary source of uncertainty in the calculation, since in that case the necessary core properties can be calculated exactly. Drachman suggested that the convergence of the asymptotic series represented by the successively higher inverse powers of r in V_{pol} could be used to estimate the truncation error in the calculation. That is, the size of the smallest calculated term may be used to estimate the possible size of remaining uncalculated terms. This approach gives an estimate of the "convergence error" in the polarization-model calculations that has recently been confirmed, in the case of helium, by high-precision variational calculations [14]. Very similar procedures can be used to estimate the convergence errors in the H$_2$ EFS calculations. These will be discussed in Sec. II, along with additional details of the application of the polarization model to the states studied here.

The finest level of structure in the high-L states is associated with the electron and proton spins. This has been treated on an *ad hoc* basis using a spin Hamiltonian that includes the effects of hyperfine interactions in the H$_2^+$ core, added to magnetic interactions with the Rydberg electron [15]. The magnetic fine structure (MFS) that results is discussed in more detail in Sec. II. We take the point of view that, to the extent that this model accounts satisfactorily for the observed MFS of the Rydberg levels, it can be used to extract from the experimental spectra information about the "pure EFS" structure. These results can then be compared directly with calculations based on the (spinless) polarization model.

An experimental method that makes possible high-resolution microwave spectroscopy of high-L H$_2$ Rydberg levels has been developed recently, and its use for the systematic study of the $n = 10$ Rydberg levels under consideration here has been briefly described [16]. In this paper, these measurements are described more completely, and an improved analysis is described in detail. Section II considers aspects of the theory of the Rydberg structure necessary for the interpretation of the measurements. Section III describes the experimental technique and the microwave measurements. Section IV compares

the experimental observations with the theoretical predictions.

II. THEORY OF RYDBERG FINE STRUCTURE

The "polarization model" can be derived from first principles, using a perturbative expansion of the nonrelativistic Coulomb Hamiltonian, as has been discussed elsewhere [10,11]. It is our purpose here to clarify the manner in which the model is used to predict the EFS of the $(0,1)10L_N$ Rydberg levels studied in this experiment. Because of the increasingly precise comparison with experiment, several points require special clarification.

A. Reduced mass corrections to V_{pol}

The calculated EFS is influenced in two ways by the finite ratio of electron to proton mass m_e/m_p. The simpler effect is the change in radial scale of the Rydberg electron wave function caused by the finite proton mass. The correct wave function is obtained from the elementary infinite-nuclear-mass wave function by the substitution

$$a_0 \rightarrow a_0(1+\epsilon) , \tag{4}$$

where $\epsilon \equiv m_e/(2m_p+m_e)$. This scaling factor is quite significant in evaluating the expectation values of the various inverse powers of the radial coordinate that appear in Eq. (1).

A second source of corrections of relative order m_e/m_p is more subtle, but follows the line of reasoning laid out by Drachman in studies of high-L helium Rydberg states [17,18]. If, as in Ref. [10], the relative coordinate of the Rydberg electron is defined with respect to the midpoint between the two protons in H_2^+, that is, the nuclear center of mass, the transformation of the kinetic-energy terms in the Hamiltonian contains "mass-polarization" terms that are normally neglected. In the closely analogous case of helium Rydberg states, it has been shown by Drachman that the effect of these terms is twofold: they produce a small "second-order mass-polarization" energy shift that is common to all Rydberg states of the same n [18], and in addition they introduce small corrections to the polarization potential of order m_e/m_p [17,12]. As shown for helium by Drachman, a far simpler procedure than directly evaluating the effects of the mass-polarization operators, which gives equivalent results, is to use a different set of coordinates, "Jacobi coordinates," in which the coordinate of the Rydberg electron is defined with respect to the center of mass of the ion core. When this is done, the mass-polarization operators do not occur in the transformed kinetic energy. Instead, the energy shifts previously associated with the mass-polarization operators appear in a different manner. The shift common to all helium Rydberg levels of the same n comes from a change in the effective Rydberg constant due to a revised reduced mass. The corrections to the polarization potential of order m_e/m_p are found, with far less effort, by evaluating the effects of small corrections, proportional to m_e/m_p, which occur in the perturbing Hamiltonian from which the polarization potential is derived. In Ref. [11], the H_2

polarization model was formulated in a similar set of Jacobi coordinates. As was the case of the helium atom, no mass-polarization operators occur with this choice. In addition to slightly altering the zeroth-order Rydberg energies because of the revised reduced mass, this coordinate choice causes the correction terms proportional to ϵ which are exhibited in Eq. (7b) of Ref. [11]. The effect of these small terms on the polarization potential, neglected in Ref. [11], is particularly significant in the two dominant terms of V_{pol} expressed in Eq. (1), the static quadrupole moment and the adiabatic dipole polarization terms. It becomes clear when the perturbing Hamiltonian V of Eq. (7b) in Ref. [11] is expanded in a multipole series. Retaining only the two lowest nonvanishing multipoles and only terms linear in ϵ, the result is

$$V \cong (1+\epsilon)\frac{r_1}{r_2^2}P_1(\cos\theta_{12}) + (1-2\epsilon)\frac{r_1^2}{r_2^3}P_2(\cos\theta_{12})$$

$$-2\frac{(\rho/2)^2}{r_2^3}P_2(\cos\theta_{2\rho}) . \tag{5}$$

When this expression for V is substituted into the derivation of the polarization potential, its effect is twofold. First, the prefactor $(1+\epsilon)$ attached to the dipole term multiples the dipole polarization terms by the factor $(1+\epsilon)^2 = 1.000\,544$. Secondly, the prefactor in the electronic quadrupole term modifies the static quadrupole potential. As discussed in Ref. [10], the quadrupole moment contains both nuclear and electronic contributions, $Q(\rho) \equiv 2(\rho/2)^2 - Q_e(\rho)$, where $Q_e(\rho)$ is defined by Eq. (13) of Ref. [10]. When the terms proportional to ϵ are included in its derivation, the nuclear contributions to Q are unaltered, while the electronic contribution is multiplied by the factor $1-2\epsilon$. The net effect is a small increase in the quadrupole potential

$$Q = 2(\rho/2)^2 - Q_e \rightarrow 2(\rho/2)^2 - (1-2\epsilon)Q_e$$

$$= Q(1+2\epsilon Q_e/Q) = 1.000\,172Q ,$$

where the value of Q_e/Q was taken from explicit evaluations [19]. Since both of these kinematic corrections alter the coefficients in V_{pol} by multiplicative factors near unity, it might be reasonable to consider adsorbing them into the *definitions* of the quantities Q, α_S, and α_T. We consider this undesirable, however, since the standard definitions of these quantities are widely accepted. Instead, maintaining the standard definitions, we explicitly include the small essentially kinematic corrections to the effective potential seen by the Rydberg electron, modifying the first two terms of Eq. (1) to read

$$V_{pol} = -1.000\,172\frac{eQ(\rho)}{r_2^3}P_2(\cos\theta)$$

$$-1.000\,544\frac{e^2}{r_2^4}\left[\frac{\alpha_S(\rho)}{2} + \frac{\alpha_T(\rho)}{3}P_2(\cos\theta)\right]$$

$$+ \cdots . \tag{6}$$

Similar corrections to higher-order terms are negligible for present purposes.

B. Core parameters and first-order polarization energies

The coefficients that occur in the polarization potential represent electric properties of the free H_2^+ ion. Each is defined with respect to a fictitious H_2^+ ion with stationary protons, and is therefore a function of the internuclear separation ρ. The permanent electric multipole moments (that is, the quadrupole moment, the hexadecapole moment, etc.) can be evaluated knowing only the ground-state electronic wave function, while the adiabatic polarizabilities (dipole polarizability, quadrupole polarizability, etc.) involve, in principle, the spectrum of excited states as well. The most complete evaluations of all of these parameters, both static moments and adiabatic polarizabilities, have been carried out by Bishop and Lam [13]. The nonadiabatic dipole polarizability β has been shown to be equivalent to the "second-moment" function in the presence of an electric field, which has also been evaluated by Bishop [10].

While the definitions of the permanent core moments in the molecule fixed frame are unambiguous, application to a particular Rydberg series also requires that they be averaged over the rotational-vibrational wave function appropriate to a particular core state. The rotational-vibrational wave function can be evaluated in various approximations. The Born-Oppenheimer approximation, which is the simplest, neglects the effect of nuclear kinetic energy on the internuclear potential. An improved approximation, the "adiabatic approximation," treats these nuclear kinetic-energy terms, which in principle mix various electronic states, in what amounts to first-order perturbation theory, and assumes, as does the simpler Born-Oppenheimer approximation, that the H_2^+ wave function contains a single electronic wave function as a factor. The exact wave function, however, actually contains a small component that admixes excited electronic states. Calculations that account for this and therefore do not make the "adiabatic wave-function" approximation are referred to as "nonadiabatic." Since the order of magnitude of the excited-state amplitude is approximately m_e/m_p, these details may be significant at the level of $1/1000$. Since, for most purposes, higher precision is not required for the core properties, the only systematic evaluations of all the necessary moments use adiabatic wave functions. Bearing in mind that nonadiabatic wave-function corrections may be required, at least for the leading terms, we nevertheless adopt the following estimates of the core moments taken from these adiabatic wave-function averages for the ($v=0$, $R=1$) state of H_2^+ [13]:

$$\langle Q \rangle_{0,1} = 1.642\,57 e a_0^2 ,$$

$$\langle \phi \rangle_{0,1} = 2.0192 e a_0^4 .$$

Evaluation of the core polarizabilities involves other complications, which are illustrated by the case of the dipole polarizabilities. The quantities that occur in the derivation of this part of the polarization potential [10] are the "branch polarizabilities," which are defined there in terms of a sum over electronically excited states of fixed rotational angular momentum R':

$$\alpha_\parallel^\gamma(R,R') \equiv -2 \sum_{\alpha,v'} \frac{|\int g_{XvR}(\rho) D_{X,\alpha\Sigma}(\rho) g_{\alpha\Sigma v',R'}(\rho) d\rho|^2}{E^0(XvR) - E^0(\alpha\Sigma v'R')} ,$$

(7a)

$$\alpha_\perp^\gamma(R,R') \equiv -2 \sum_{\alpha,v'} \frac{|\int g_{XvR}(\rho) D_{X,\alpha\Pi}(\rho) g_{\alpha\Pi v'R'}(\rho) d\rho|^2}{E^0(XvR) - E^0(\alpha\Pi v'R')} ,$$

(7b)

with

$$D_{X,\alpha\Lambda}(\rho) \equiv e \int f_X^*(\mathbf{r}_1';\rho) r_1 C_{-\Lambda}^1(\hat{\mathbf{r}}_1') f_{\alpha\Lambda}(\mathbf{r}_1';\rho) d^3 r_1' .$$

It can be shown that the scalar and tensor dipole polarizabilities that occur in V_{pol} can be written without approximation in terms of these branch polarizabilities [20]. For instance, in the particular case of the $R=1$ states of H_2^+, such as those studied here, it is found that

$$\alpha_S(v,R=1) = \tfrac{2}{9}\alpha_\parallel^\gamma(1,2) + \tfrac{1}{9}\alpha_\parallel^\gamma(1,0)$$
$$+ \tfrac{1}{3}\alpha_\perp^\gamma(1,2) + \tfrac{1}{3}\alpha_\perp^\gamma(1,1) ,$$

(8a)

and

$$\alpha_T(v,R=1) = \tfrac{1}{6}\alpha_\parallel^\gamma(1,2) + \tfrac{5}{6}\alpha_\parallel^\gamma(1,0)$$
$$+ \tfrac{1}{4}\alpha_\perp^\gamma(1,2) - \tfrac{5}{4}\alpha_\perp^\gamma(1,1) .$$

(8b)

Notice that if the dependence of the branch polarizabilities on R' were neglected, these would reduce to the standard forms

$$\alpha_S = \frac{\alpha_\parallel + 2\alpha_\perp}{3}$$

and

$$\alpha_T = \alpha_\parallel - \alpha_\perp .$$

Since the branch polarizabilities of H_2^+ have never been calculated, it is fortunate that their dependence on R' is expected to be slight. The standard approximation for the dipole polarizabilities can be recovered by setting

$$E^0(XvR) - E^0(\alpha\Lambda v'R') \equiv E_X(\rho) - E_{\alpha\Lambda}(\rho)$$

in the denominator of Eq. (7). The right-hand side of this expression is the difference of potential curves for the ground (X) and electronically excited ($\alpha\Lambda$) states of H_2^+. In this approximation, using the completeness of the rotational-vibrational functions $g_{\alpha\Lambda v'R'}(\rho)$, it is found that

$$\alpha_\parallel^\gamma(R,R') \cong \int |g_{XvR}(\rho)|^2 \alpha_\parallel(\rho) d\rho ,$$

(9a)

$$\alpha_\perp^\gamma(R,R') \cong \int |g_{XvR}(\rho)|^2 \alpha_\perp(\rho) d\rho ,$$

(9b)

where

$$\alpha_\parallel(\rho) \equiv -2 \sum_\alpha \frac{|D_{X,\alpha\Sigma}(\rho)|^2}{E_X(\rho) - E_{\alpha\Sigma}(\rho)} ,$$

and

$$\alpha_\perp(\rho) \equiv -2 \sum_\alpha \frac{|D_{X,\alpha\Pi}(\rho)|^2}{E_X(\rho) - E_{\alpha\Pi}(\rho)}$$

are the usual "clamped-nucleus" forms of the dipole polarizabilities, evaluated as a function of internuclear separation. Since all dependence of the branch polarizabilities on R' is lost in this approximation, the usual relationship to α_S and α_T is also recovered. The important point to note is that the assumption that the polarizabilities can be evaluated for clamped nuclei and subsequently averaged over rotational-vibrational wave functions is already an approximation. The error that it introduces is probably less than 1%, judging from discussions of related problems [21], but is almost certainly greater than 0.1%. Similar considerations apply to all the other polarizabilities, but are probably insignificant for present purposes except in the case of the dipole polarizabilities.

The clamped-nucleus polarizabilities, both dipole and higher order, have been systematically evaluated by Bishop and collaborators using variational techniques. As in the case of the permanent moments, the choice of the rotational-vibrational wave function for the averaging of these polarizabilities involves further approximations. The best available numbers for the (0,1) state of $H_2{}^+$ are obtained by averaging over the adiabatic rotational-vibrational wave function and are given by

$$\langle \alpha_S \rangle_{0,1} = 3.180\,88a_0^3 \, ,$$

$$\langle \alpha_T \rangle_{0,1} = 4.027\,31a_0^3 \, ,$$

$$\langle C_0 \rangle_{0,1} = 24.066a_0^5 \, ,$$

$$\langle C_1 \rangle_{0,1} = 5.118a_0^5 \, ,$$

$$\langle C_2 \rangle_{0,1} = 0.420a_0^5 \, ,$$

$$\langle E_1 \rangle_{0,1} = 26.77a_0^5 \, ,$$

$$\langle E_2 \rangle_{0,1} = 14.6a_0^5 \, ,$$

$$\langle \beta_S \rangle_{0,1} = 6.84a_0^4/e^2 \, ,$$

and

$$\langle \beta_T \rangle_{0,1} = 12.49a_0^4/e^2 \, .$$

These values are all taken from calculations by Bishop [13], and are similar to those cited in Ref. [11] except that a sign error in the value of the Cartesian component of the E tensor, $E_{x,xxx}$, cited in Ref. [10] has been corrected. The correct value is

$$\langle E_{x,xxx} \rangle_{0,1} = -1.130a_0^5 \, .$$

This alters the derived spherical components E_1 and E_2 as indicated in Eq. (38) of Ref. [10]. As discussed in Ref. [11], the values of the quadrupole polarizabilities C differ from those cited in Ref. [10] since only the electronic contributions to the quadrupole polarizabilities are appropriate to include here. The values of β_S and β_T are obtained from the S_{-3} moment function calculations by Bishop [22].

The first-order polarization energies for the $(0,1)10L_N$ states studied here are of the form

$$E_{\text{pol}}^{[1]} = A_0(v,R,n,L) + A_2(v,R,n,L)$$

$$\times \langle R,L;N|P_2(\cos\theta)|R,L;N \rangle \, ,$$

(10)

since terms in V_{pol} proportional to $P_4(\cos\theta)$ give zero expectation value in the $R = 1$ core state. The scalar (A_0) and tensor (A_2) structure factors can be evaluated from the expectation value of the appropriate terms in V_{pol}. An estimate of the error incurred by neglecting higher-order terms in the expansion is found from the size of the smallest calculated term. Following Drachman [12], we group together all terms proportional to r^{-s} and denote their total contribution V_s. Then we estimate the parameters A_0 and A_2 by

$$A = V_3 + V_4 + V_6 + (-\tfrac{1}{2}V_6 \pm \tfrac{1}{2}V_6) \, ,$$

(11)

where the last term is an estimate of the contribution of uncalculated higher-order terms. The values of A_0 and A_2 predicted in this way for the states under study, using

TABLE I. Polarization-model predictions of the scalar (A_0) and tensor (A_2) structure factors of $(0,1)10L$ states of H_2 with $4 \le L \le 7$. Numbers in parenthesis are one-standard-deviation error estimates, based on the estimate of uncalculated higher terms as $(-\tfrac{1}{2}\pm\tfrac{1}{2})$ times the total calculated r^{-6} contribution. All units are MHz.

$-s$	Coefficient	$10G$	$10H$	$10I$	$10K$
4	α_S	-8451.6	-2925.5	-1198.5	-549.9
6	β_S	488.0	63.0	11.4	2.4
6	C_0	-114.4	-14.8	-2.6	-0.6
>6 (estimate)		$-186.8(1868)$	$-24.1(241)$	$-4.4(44)$	$0.9(9)$
A_0 (total):		$-8265(187)$	$-2901(24)$	$-1193.7(44)$	$-549.0(9)$
3	Q	$-120\,005.2$	$-65\,457.4$	$-39\,562.2$	$-25\,715.4$
4	α_T	-7133.7	-2469.4	-1011.3	-464.1
6	β_T	297.0	38.4	6.8	1.6
6	C_1	-34.8	-4.4	-0.8	-0.2
6	E_1	-182.0	-23.4	-4.2	-1.0
>6 (estimate)		$-40.1(401)$	$-5.3(53)$	$0.9(0)$	$-0.2(2)$
A_2 (total):		$-127\,099(40)$	$-67\,922(5)$	$-40\,572.6(9)$	$-26\,179.3(2)$

the radial expectation values given by Bockasten [23] corrected for finite core mass, and with the above choice of core parameters, are shown in Table I. These differ from the values shown in Table III of Ref. [16] because of (a) the inclusion of the finite nuclear mass corrections to the α and Q terms, discussed above and shown in Eq. (6), and (b) the use of different values of the C and E tensor coefficients.

C. Second-order polarization energies

The second-order polarization energies, defined in Eq. (3), for each of the states studied here, were computed from the expression

$$E_{\text{pol}}^{[2]}[(v,R)nL_N]$$

$$= \sum_{v',R',n',L'} \frac{|\langle (v,R)nL_N|V_{\text{pol}}|(v'R')n'L_N'\rangle|^2}{\Delta E} ,$$

(12)

where

$$\Delta E \equiv E^{[0]}((v,R)nL_N) + E_{\text{pol}}^{[1]}((v,R)nL_N)$$

$$- E^{[0]}((v',R')n'L_N') - E_{\text{pol}}^{[1]}((v',R')n'L_N') .$$

(13)

This use of the polarization potential is discussed in Ref. [11]. The choice of energy denominator is designed to correct for the first-order polarization energies in computing mixing to nearly degenerate levels, as discussed there. The sum over n' includes both discrete and continuum levels of given L and N. The matrix elements of V_{pol} between Rydberg states in different series, required for these computations, involve matrix elements of the various core parameters between different rotational-vibrational states of H$_2{}^+$. We estimated these from tables of matrix elements off diagonal in v only [24], using the expression

$$\langle vR|f(\rho)|v'R'\rangle$$

$$\cong |\langle vR|f(\rho)|v'R\rangle\langle vR'|f(\rho)|v'R'\rangle|^{1/2} .$$

(14)

For the most significant matrix elements, those with $v=v'$, this approximation is expected to be accurate to 0.1%. It may be less accurate for $v\neq v'$, but these matrix elements are far less significant. A typical breakdown of second-order polarization energies by perturbing series is given in Table VI of Ref. [10]. An estimate of the precision of the calculation of $E^{[2]}$ by this prescription may be obtained by grouping terms in the numerator product according to the total inverse power of r, which ranges from r^{-6} for the QQ mixing term to r^{-9} for the $\alpha\phi$ mixing term. Terms with total power r^{-10}, like $\phi\phi$, are dropped, since other terms of potentially the same magnitude are omitted when V_{pol} is truncated after r^{-6}. The total energy shift is estimated from

$$E^{[2]} \cong (V_6 + V_7 + V_8 + V_9) \pm \tfrac{1}{2}V_9 ,$$

(15)

where V_6, etc., is the total contribution from all terms proportional to r^{-6}, etc., summed over all intermediate states. The contributions from discrete and continuum intermediate states were evaluated separately. The shifts due to discrete levels were estimated by explicitly evaluating the contributions of all discrete levels with $n'\leq 45$, and extrapolating to account for the contributions of all remaining discrete levels. The contribution from continuum levels was estimated by calculating the contributions of a number of representative continuum levels in the energy range 0–0.6 a.u. At the highest energy, the contributions were found to decrease smoothly, and were fit to a power law to estimate the integrated contribution from all continuum states. The resulting values of the second-order polarization energies for the states under study are shown in Table II. These are in satisfactory agreement with the values given in Ref. [16], and are somewhat more precise because of our inclusion of mixing terms up to r^{-9}, compared to only r^{-8} in that work.

TABLE II. Second-order polarization energies of $(0,1)10L_N$ states of H$_2$, calculated from Eq. (12) in the text. The total contribution by other bound, discrete states is labeled $E_{\text{pol},d}^{[2]}$, while $E_{\text{pol},c}^{[2]}$ is the total contribution by the various continua. The sum of these two is listed in the last column, $E_{\text{pol}}^{[2]}$. All units are MHz. The numbers in parenthesis are one-standard-deviation estimates, obtained from Eq. (15).

State	$E_{\text{pol},d}^{[2]}$	$E_{\text{pol},c}^{[2]}$	$E_{\text{pol}}^{[2]}$
G_3	24.6(12)	−454.4(34)	−429.8(36)
G_4	−726.6(12)	−277.0(39)	−1003.6(41)
G_5	−533.4(8)	−413.9(19)	−947.3(21)
H_4	−28.78(2)	−82.46(14)	−111.24(15)
H_5	−218.59(4)	−56.35(17)	−274.94(17)
H_6	−155.00(2)	−78.50(9)	−233.50(10)
I_5	−17.07	−20.12(1)	−37.18(1)
I_6	−76.82	−13.21(1)	−90.03(1)
I_7	−52.51	−19.80(1)	−72.31(1)
K_6	−10.65	−5.50	−16.15
K_7	−29.21	−3.21	−32.42
K_8	−21.55	−5.60	−27.15

D. Magnetic fine structure

The MFS Hamiltonian was discussed in Ref. [15], and, in more detail, in Ref. [11]. It was developed in an *ad hoc* fashion by including what are expected to be the most significant spin interactions, and can be expressed as

$$H^{\mathrm{MFS}} = H_{\mathrm{hyp}} + H_{\mathrm{mag}} + H_X \ , \tag{16}$$

where

$$H_{\mathrm{hyp}} = b(\mathbf{I}\cdot\mathbf{S}_1) + c(\mathbf{I}\cdot\hat{\rho})(\hat{\rho}\cdot\mathbf{S}_1) + d(\mathbf{R}\cdot\mathbf{S}_1) \ , \tag{17}$$

$$\frac{\mathcal{R}}{3}\{L\cdot\mathbf{S}_2 - 2L\cdot\mathbf{S}_1 + 2\mathbf{S}_2\cdot[\mathbf{S}_1 - 3\hat{r}(\hat{r}\cdot\mathbf{S}_1)]\} \ , \tag{18}$$

$$H_x = -V_x(\tfrac{1}{2} + 2\mathbf{S}_1\cdot\mathbf{S}_2) \ . \tag{19}$$

The constants in Eq. (17), b, c, and d, are the calculated hyperfine constants for the free H_2^+ ion in the appropriate rotational-vibrational state (v,R), for which we take the values $b = 880.551$, $c = 128.432$, and $d = 42.399$ [25]. The unit vector along the internuclear axis is denoted $\hat{\rho}$, $\mathbf{I}$ is the total nuclear spin, $\mathbf{S}_1$ is the spin of the core electron, and $\mathbf{S}_2$ is the spin of the Rydberg electron. Also, α is the fine-structure constant, and $\mathcal{R}$ is the Rydberg constant. The parameter V_x represents the exchange energy, which if all other spin interactions were negligible, would be half the difference in energy between two-electron spatial wave functions of even and odd exchange symmetry. Since the other interactions dominate the observed structure, the exchange energy plays a very minor role in the magnetic fine structure of the states studied here. A corrected analysis of data from a previous study [15] indicates that

$$V_x(10G) \cong 0.30(10) \ \mathrm{MHz} \ .$$

Since V_x is expected to decrease rapidly for higher-L states, we take $V_x = 0.00$ MHz for all $n = 10$ Rydberg levels with $L > 4$.

One may contrast the *ad hoc* status of the MFS Hamiltonian to the EFS Hamiltonian [Eq. (1)], which was derived in a rigorous manner from the nonrelativistic Hamiltonian. We have no theoretical estimate of the MFS errors, nor of the limits of applicability of the MFS model. The degree of agreement between the model and the many spectroscopically measured transitions provides our only estimate of error. Previous measurements indicate that the model agrees with observations at about the 1% level [11,15], and we find similar results below.

In order to evaluate Eqs. (16)–(19), we note that, when the EFS is much larger than the MFS, the MFS Hamiltonian is approximately diagonal in a basis characterized by $(v,R)nL_N$, the EFS state; $\mathbf{I} = \mathbf{I}_1 + \mathbf{I}_2$, the total proton spin, required by symmetry to be 1 (odd R) or 0 (even R); $\mathbf{F} = \mathbf{I} + \mathbf{S}_1$, the total core spin; $\mathbf{J}_1 = \mathbf{N} + \mathbf{F}$, an intermediate angular momentum; and $\mathbf{J} = \mathbf{J}_1 + \mathbf{S}_2$, the total angular momentum. We denote these basis states $(v,R,F)nL_N(J_1,J)$. The notation (v,R,F) anticipates the observation that the difference in energy between $F = 1.5$ and $F = 0.5$ is most naturally considered part of the H_2^+ core energy.

In Ref. [11] it was shown that when $n > 25$ and the electric fine structure is comparable to the MFS energy, it was necessary to treat H^{MFS} as an effective Hamiltonian and diagonalize it within a subspace of Rydberg levels of a given core state (v,R) and a fixed nL. Because the electric fine structure is so much larger in this study, the diagonalization is not necessary, and the small perturbations caused by nearby states can be treated by second-order perturbation theory. That is,

$$E_{\mathrm{MFS}}^{[1]} = \langle (v,R,F)nL_N(J_1,J)|H^{\mathrm{MFS}}|(v,R,F)nL_N(J_1,J)\rangle \ , \tag{20}$$

$$E_{\mathrm{MFS}}^{[2]} = \sum_{F'J'N'} \frac{|\langle (v,R,F)nL_N(J_1,J)|H^{\mathrm{MFS}}|(v,R,F')nL_{N'}(J_1',J)\rangle|^2}{(\Delta E)^*} \ , \tag{21}$$

where

$$(\Delta E)^* = E_{\mathrm{pol}}[(v,R)nL_N] + E_{\mathrm{MFS}}^{[1]}[(v,R,F)nL_N(J_1,J)]$$
$$- E_{\mathrm{pol}}[(v,R)nL_{N'}]$$
$$- E_{\mathrm{MFS}}^{[1]}[(v,R,F')nL_{N'}(J_1',J)] \ , \tag{22}$$

and the total energy of the state is

$$E_{\mathrm{tot}} = E^0 + E_{\mathrm{pol}} + E_{\mathrm{MFS}}^{[1]} + E_{\mathrm{MFS}}^{[2]} \ , \tag{23}$$

where E_{pol} is the sum of first- and second-order polarization energies [Eqs. (2) and (3)]. Explicit representations of the MFS matrix elements between any two states, for each term in Eqs. (16)–(19), are listed in Appendix A. Also listed in the Appendix are the selection rules of each operator, along with a sample table giving explicit calculations for one Rydberg state, the $(0,1)10H$ state.

A particular fine-structure transition, such as $(0,1)10G_5$-$(0,1)10H_6$, is actually a superposition of transitions between specific MFS levels, with those transitions having the strongest electric dipole matrix elements dominating the pattern at low microwave power. An explicit representation of the dipole matrix elements in our basis set is given in the Appendix. The matrix elements (be-

tween basis states) satisfy the rigorous selection rule $\Delta I = 0$ and $\Delta F = 0$, and $\Delta J = 0, \pm 1$. The approximate selection rule $\Delta J = \Delta J_1 = \Delta N$ is also found to hold. The largest dipole matrix elements are between the states that satisfy $\Delta N = \Delta L$. The MFS of these states is quite similar, so that the resultant 12 transitions have very similar frequencies. Given the resolution of this experiment, these transitions appear as a single peak. Slightly weaker transitions occur when $\Delta N = 0$, such as $(0,1)10H_6$-$(0,1)10I_6$. These states do not have a similar magnetic fine structure, however, and the resultant transitions appear as several partially resolved peaks. Since $\Delta F = 0$ remains a good selection rule, the dipole hyperfine structure, the first term in Eq. (17), does not contribute to the splittings, and the peaks are spread out over frequencies comparable to the remaining MFS, typically 50–100 MHz.

III. EXPERIMENT

The experimental apparatus is shown schematically in Fig. 1. A fast beam of neutral H_2 is prepared by charge exchange from an 11.16(5) keV beam of H_2^+, which is produced by a conventional duoplasmatron ion source. The mass-selected H_2^+ beam is partially neutralized in a gas cell containing a few millitorr of argon gas. The resulting neutral beam contains many highly excited Rydberg states, including the $n = 10$ states studied here. Any remaining positive ions and Rydberg states with $n \geq 24$ are removed from the beam with a strong deflection field immediately following the charge exchange cell. Specific Rydberg levels still present in the beam may be selectively detected by resonant laser excitation to a very-weakly-bound discrete level (e.g., $n = 30$), followed by Stark ionization of the upper level and collection of the resulting

ion. This process is particularly convenient for $n = 10$ Rydberg levels, where the laser excitation can be accomplished with a Doppler-tuned cw CO_2 laser. For a beam of this velocity $[v/c \cong 0.003\,448(7)]$, a range of discretely tunable CO_2 lines gives continuous frequency coverage with Doppler tuning. The $n = 10$ excitation spectrum observed in this way [26] shows well-resolved fine structure due to the Rydberg fine structure of the $n = 10$ levels, and allows the selective excitation and detection of numerous $n = 10$ H_2 Rydberg levels with $L = 3$, 4, 5, and 6 bound to H_2^+ in $v = 0$, $R = 0$, 1, 2, and 3 states. With the Doppler-tuned laser frequency adjusted to excite one particular $n = 10$ Rydberg level, e.g., the $(0,1)10G_5$ level, the resulting ion current after Stark ionization is a measure of the population of this particular level, and it can therefore be used to detect microwave-induced transitions between this level and any other $n = 10$ Rydberg level. The first use of this technique to detect the $(0,1)10G_5$-$(0,1)10H_6$ transition has been described previously [15]. For this study, we have extended the technique to study the ten different fine-structure transitions within the $(0,1)10L$ system that are illustrated in Fig. 2. Table III lists the transitions studied along with their approximate frequencies. Also listed for each transition is the optical transition used to detect it and an identification code for the microwave interaction region in which the transition was driven. For all of these signals, the naturally occurring population differences between the various fine-structure levels were sufficient for observation of the signals, and therefore no steps were taken to artificially induce a larger population difference.

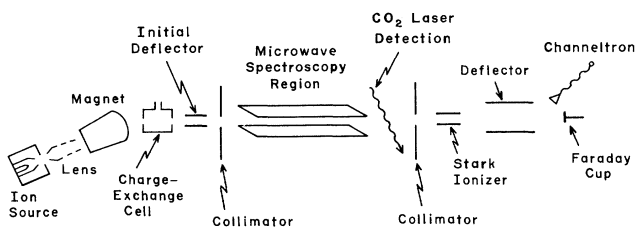Figure 3 illustrates the microwave interaction regions that were used to drive these transitions. Four different

FIG. 1. Schematic diagram of the fast-beam microwave-optical apparatus. An accelerated beam of H_2^+ ions forms a fast neutral-H_2 beam by charge exchange. After the charge exchange cell, residual ions are swept out of the beam. Particular $n = 10$ fine-structure levels are excited by a Doppler-tuned CO_2 laser to a very-highly-excited discrete state (typically $n = 30$) which is then immediately Stark ionized. The resulting ions, detected by a channeltron, provide a measure of the population of one $n = 10$ fine-structure level, and reveal population changes induced by resonant microwave transitions to other fine-structure levels.
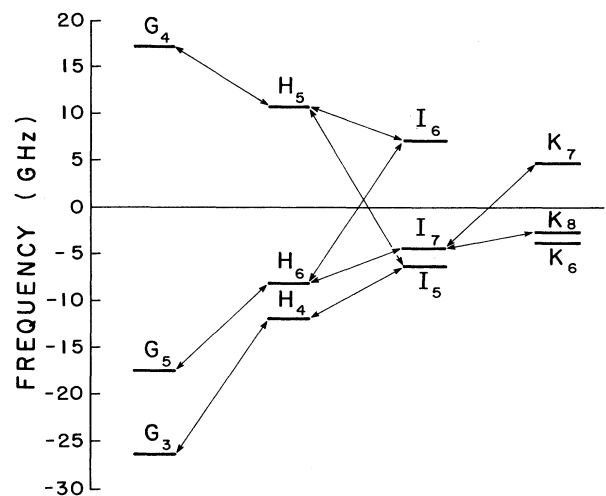

FIG. 2. Level diagram illustrating the electric fine structure of the H_2 Rydberg states studied in this experiment, the $(0,1)10L_N$ states with $4 \leq L \leq 7$. The arrows show the fine-structure transitions that have been studied here. The MFS, which is due to the electron and proton spins, is not shown.

TABLE III. Fine-structure transitions observed in this study. For each microwave transition is listed the frequency range of the spectrum, the optical transition used for detection, and the microwave interaction region used. The characteristics of each region are defined in Table IV.

Transition	Frequency (MHz)	Optical transition	Microwave region
$10G_3 \to 10H_4$	14 675–14 775	$10G_3 \to 27H_4$	P band
$10G_4 \to 10H_5$	5 805–5 860	$10G_4 \to 27H_5$	G band
$10G_5 \to 10H_6$	9 995–10 070	$10G_5 \to 27H_6$	X band
$10H_4 \to 10I_5$	5 640–5 690	$10H_4 \to 27I_5$	G band
$10H_5 \to 10I_6$	3 575–3 605	$10H_5 \to 27I_6$	G band
$10H_6 \to 10I_7$	3 820–3 855	$10H_6 \to 27I_7$	G band
$10I_7 \to 10K_8$	1 765–1 795	$10I_7 \to 27K_8$	coaxial
$10H_5 \to 10I_5$	16 720–16 920	$10H_5 \to 27I_6$	P band
$10H_6 \to 10I_6$	15 090–15 290	$10H_6 \to 27I_7$	P band
$10I_7 \to 10K_7$	9 140–9 260	$10I_7 \to 27K_8$	X band

regions were used, whose characteristics are given in Table IV. Three of the regions were waveguide transmission lines, similar to that shown in Fig. 3(a), while the fourth, illustrated in Fig. 3(b), was a coaxial region similar to that used in studies of atomic helium Rydberg levels [27,28]. In each case, the fast H_2 passes through the region along the axis of microwave propagation, either parallel or antiparallel to the direction of microwave propagation. The resonance linewidth expected in in-

FIG. 3. Two types of microwave interaction regions used in this experiment: (a) constructed from a conventional waveguide, and (b) a specially constructed section of TEM transmission line. The relevant physical dimensions of all the regions are given in Table IV.

teractions with the fast beam is limited by the transit time of the beam through the region, and is given approximately by

$$\Delta \nu_T = 1/T = v/L ,$$

where L is the length of the region, given in Table IV, and v is the beam velocity. For the geometries listed in Table IV and the beam speed used, $\Delta \nu_T$ ranges from 3 to 8 MHz. One of the significant properties of each region is the reflection coefficient of its output port, since this determines the extent to which the microwave field is a pure traveling wave. Table IV lists approximate values for these coefficients in the frequency range used.

Another significant characteristic of the microwave interaction regions is the electric and magnetic field environment within them. For most of the fine-structure resonances studied here, no effort was made to eliminate the earth's magnetic field within the interaction region. Consequently, in most cases an approximately vertical magnetic field of magnitude 0.30 G was present throughout each region, along with the associated motional electric field, 0.31 V/cm. The exception was the coaxial region, which incorporated magnetic shielding to reduce the ambient magnetic field to 0.06 G. Other electric fields within the interaction regions, perhaps due to charge buildup on their normally conducting surfaces, were assumed to be smaller than the motional fields.

Figure 4 shows typical data for two of the transitions studied, $G_4 \to H_5$ and $I_7 \to K_7$. Two other resonance line shapes, $H_6 \to I_7$ and $H_6 \to I_6$, are illustrated in our earlier report [16]. For all but one of the transitions studied, $I_7 \to K_7$, the resonance line shape was measured for both directions of propagation of the microwave traveling wave, parallel and antiparallel to the molecular-beam velocity. For the strongest transitions, those with $\Delta N = \Delta L$ as in Fig. 4(a), the similar MFS of the two levels leads to a predicted substructure that is rather closely spaced, as illustrated by the stick diagram in Fig. 4(a), and which at the resolution of this experiment ($\Delta \nu_T = 5.3$ MHz for this region) results in a composite line shape that appears as a single resonance. These resonances were analyzed by fitting them to a single Gaussian peak, varying position, height, and width, along with a linear background. On the other hand, the transitions with $\Delta N = 0$, as in Fig. 4(b), connect states of very different MFS, giving rise to a composite line shape which at our instrumental resolution appears as four separate peaks. This data was analyzed by fitting it to a superposition of four Gaussians of common width, varying the individual peak heights and positions along with a constant background. The peak positions resulting from all of these fits are shown in the first column of Tables V and VI.

As a first step in the analysis of this data, the results from the two directions of propagation were combined to eliminate the Doppler shift and to determine the equivalent resonance position for stationary molecules. Inside a uniform section of waveguide, a beam propagating along the waveguide axis sees a Doppler-shifted microwave frequency given by
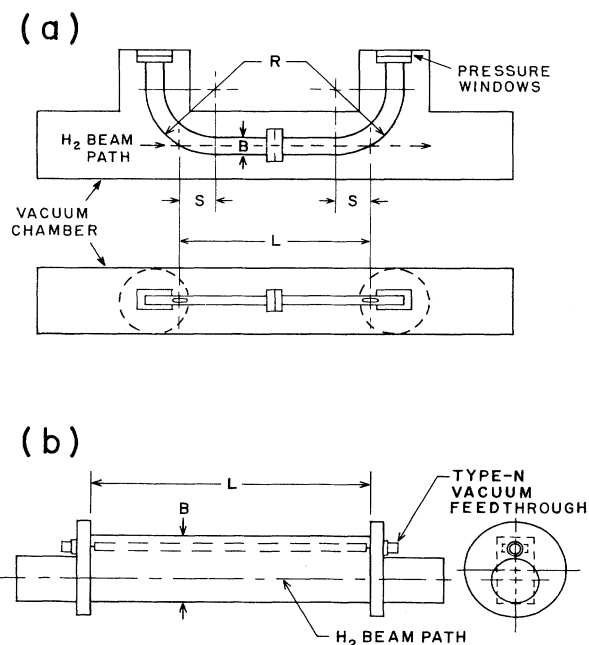
TABLE IV. Characteristics of the microwave interaction regions used in this experiment. The geometries are illustrated in Fig. 3. For each region is listed the dimension of the largest side B, the length of the region L, the distance from the entrance aperture to the straight section of the region S, and the radius of curvature of the ends R. Γ is the measured voltage reflection coefficient from one end of the region.

Region	B (cm)	L (cm)	S (cm)	R (cm)	Γ
Coaxial	7.214	29.5			$\simeq 0.15$
G band	4.755	19.4	8.52	7.29	$\simeq 0.30$
X band	2.286	13.1	4.58	8.64	$\simeq 0.15$
P band	1.580	17.1	1.83	4.76	$\simeq 0.10$

$$\nu' = \frac{\nu}{(1-\beta^2)^{1/2}}(1\pm\beta\lambda_0/\lambda_g) , \tag{24}$$

where

$$\lambda_0/\lambda_g = (1-(\nu_c/\nu)^2)^{1/2} , \tag{25}$$

FIG. 4. Two examples of microwave resonance line shapes observed in this experiment: (a) the $G_4 \rightarrow H_5$ transition, and (b) the $I_7 \rightarrow K_7$ transition. Resonance (a) was obtained with fast-beam and microwave traveling-wave counter propagating, while resonance (b) was taken with copropagating directions. Resonance (a) is an example of a $\Delta N = 1$ transition, for which the substructure due to MFS is unresolved, as illustrated by the stick diagram showing the predicted substructure. Resonance (b) illustrates the case of a $\Delta N = 0$ transition, which shows partially resolved MFS.

with $\beta = v/c$ and $\nu_c = c/2B$, where c is the speed of light and B is the waveguide dimension tabulated in Table IV. (For the TEM coaxial interaction region, $\nu_c = 0$.) In practice, for interaction regions constructed as in Fig. 3(a), the Doppler shift is expected to be somewhat smaller than this due to the influence of the bend regions, where the microwave propagation direction turns gradually away from the molecular-beam velocity. Corrections to the Doppler shifts due to these bend regions can be included by introducing a factor $f_B \cong 1$ into Eq. (24). As a result, we expect the up- and down-shifted resonance frequencies $(\nu^{\pm})$ to be given in terms of ν_0, the resonance frequency for stationary atoms, by

$$\nu_0 = \frac{\nu^{\pm}}{(1-\beta^2)^{1/2}}[1 \mp f_B\beta(\lambda_0/\lambda_g)] . \tag{26}$$

It follows that measurements of $\nu^{\pm}$ determine both ν_0 and f_B according to

$$\nu_0 = \bar{\nu}[1+\beta^2(\tfrac{1}{2}-f_B^2)+O(\beta^4)] \tag{27}$$

and

$$f_B \cong \frac{\nu^+ - \nu^-}{2\bar{\nu}\beta}[1-(\nu_c/\bar{\nu})^2]^{-1/2} , \tag{28}$$

where

$$\bar{\nu} \equiv \frac{\nu^+ + \nu^-}{2} .$$

Tables V and VI show the values of f_B and ν_0 obtained for each transition.

The values of f_B may be compared with a simple calculation based on the waveguide geometry. Following the treatment used elsewhere [29], a local Doppler-shifted frequency $\nu'(s)$ is defined for all points along the beam trajectory as determined by the local angle between the beam velocity and the waveguide axis. The "average" Doppler shifted frequency ν'_A is then computed from

$$\nu'_A = \frac{\int |E(s)|^2\nu'(s)ds}{\int |E(s)|^2ds} , \tag{29}$$

The electric field $E(s)$ is approximated by the single TE_{10} mode throughout the bend region. For the geometries of Table IV, this calculation predicts
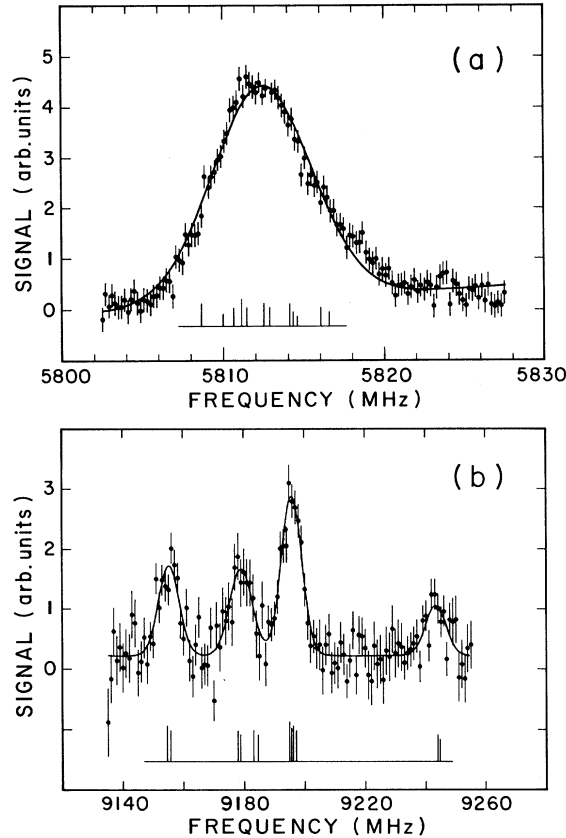
$$f_B = \begin{cases} 0.977 & (G \text{ band}) \\ 0.987 & (X \text{ band}) \\ 0.995 & (P \text{ band}) \,. \end{cases}$$

Of course, on this same basis, the coaxial region would be expected to give

$$f_B = 1.0 \quad (\text{coaxial}) \,.$$

Comparison with the observed values of f_B, shown in Tables V and VI, shows good agreement for the P band, but rather poor agreement for the other regions. In the case of the G-band region, f_B shows a systematic dependence on frequency, and appears to converge towards the predicted value for $v \gg v_c$. The coaxial region also shows a clear deviation from the prediction. In the case of the waveguide regions, these observations are similar to the results of other studies [29]. These discrepancies may be due to the influence of nonpropagating electromagnetic modes in the bend or transition regions, which are neglected in the simple model used to predict f_B. Fortunately, when computed according to Eq. (27), v_0 is rather insensitive to the precise value of f_B. In the one case where resonances for both directions of microwave propagation were not measured $(I_7 \rightarrow K_8)$, f_B was estimated as 0.967(9) from the $G_5 \rightarrow H_6$ results, and

TABLE V. The experimentally measured $\Delta N = 0$ transitions. Each transition has four resolvable composite peaks (1)–(4) whose fitted positions, for both directions of microwave propagation (A,B), are listed in the fourth column. From these two measured frequencies, both the resonance position for stationary atoms (v_0) and the Doppler-shift factor (f_B) can be computed as described in the text, and are shown for each transition in columns six and five, respectively. Column seven lists Δv_{MFS}, the calculated correction to each resonance position due to magnetic fine structure to obtain v_{EFS}, the pure electric fine structure interval. Columns eight and nine show the systematic corrections and uncertainties due to Stark shifts and microwave reflections, respectively. The resulting values of v_{EFS} are shown in column ten, with the associated statistical uncertainty. The average value of v_{EFS} from the four independent measurements of each interval is also shown in column ten, including an additional ± 0.10-MHz uncertainty due to possible inaccuracies in the MFS model, and including other systematic uncertainties. The numbers in parenthesis are one-standard-deviation estimates. Except for f_B, which is dimensionless, the units are MHz. Values denoted by an asterisk were estimated from the observed $G_5 \rightarrow H_6$ Doppler shift.

Transition	Peak	Direction	v_{fit}	f_B	v_0	Δv_{MFS}	Δv_S	Δv_r	v_{EFS}
$H_5 \rightarrow I_5$	(1)	A	16 839.92(20)						
				0.997(4)	16 792.22(15)	26.39	−0.08(0)	0.00(0)	16 818.53(15)
		B	16 744.71(21)						
$H_5 \rightarrow I_5$	(2)	A	16 860.65(29)						
				1.006(5)	16 812.41(21)	5.89	−0.08(0)	0.00(0)	16 818.22(21)
		B	16 764.37(29)						
$H_5 \rightarrow I_5$	(3)	A	16 873.59(23)						
				0.991(4)	16 826.01(16)	−7.57	−0.08(0)	0.00(0)	16 818.36(16)
		B	16 778.63(22)						
$H_5 \rightarrow I_5$	(4)	A	16 905.32(27)						
				0.989(5)	16 857.72(20)	−39.09	−0.08(0)	0.00(0)	<u>16 818.55(20)</u>
		B	16 810.32(28)						
								Average v_{EFS}:	16 818.42(14)
$H_6 \rightarrow I_6$	(1)	A	15 187.24(22)						
				0.993(4)	15 146.74(14)	35.72	−0.09(0)	0.00(0)	15 182.37(14)
		B	15 106.41(18)						
$H_6 \rightarrow I_6$	(2)	A	15 214.18(23)						
				0.999(4)	15 173.29(16)	8.62	−0.09(0)	0.00(0)	15 181.82(16)
		B	15 132.57(22)						
$H_6 \rightarrow I_6$	(3)	A	15 228.44(9)						
				0.997(4)	15 187.59(7)	−5.57	−0.09(0)	0.00(0)	15 181.93(7)
		B	15 146.91(10)						
$H_6 \rightarrow I_6$	(4)	A	15 277.66(21)						
				0.995(4)	15 236.65(13)	−54.36	−0.09(0)	0.00(0)	<u>15 182.20(13)</u>
		B	15 195.82(16)						
								Average v_{EFS}:	15 182.08(16)
$I_7 \rightarrow K_7$	(1)	A	9 155.27(33)	0.967(9)*	9 134.02(33)	35.20	−0.09(0)	0.00(15)	9 169.13(33)
$I_7 \rightarrow K_7$	(2)	A	9 179.05(53)	0.967(9)*	9 157.69(53)	9.50	−0.09(0)	0.00(15)	9 167.10(53)
$I_7 \rightarrow K_7$	(3)	A	9 195.69(20)	0.967(9)*	9 174.25(20)	−5.52	−0.09(0)	0.00(15)	9 168.64(20)
$I_7 \rightarrow K_7$	(4)	A	9 243.29(59)	0.967(9)*	9 221.62(59)	−53.44	−0.09(0)	0.00(15)	<u>9 168.09(59)</u>
								Average v_{EFS}:	9 168.24(51)

TABLE VI. Measured $\Delta N = 1$ electric-fine-structure transitions. For each transition there is only one composite peak, measured in two different propagation directions: copropagating (A), and counterpropagating (B). The results of the single-Gaussian fit are listed for each direction, from which the Doppler factor f_B and the Doppler-free line center ν_0 are tabulated as in Table V. To this are applied systematic corrections due to magnetic fine structure ($\Delta\nu_{\mathrm{MFS}}$), Stark shift ($\Delta\nu_S$), and reflected wave ($\Delta\nu_r$). The final electric-fine-structure interval estimate is listed in the last column. Units are MHz. The numbers in parenthesis are one-standard-deviation estimates. The result for the $G_5 \rightarrow H_6$ transition is in satisfactory agreement with a previous measurement of Ref. [15] [10 031.24(10) MHz].

Transition	Direction	ν_{fit}	f_B	ν_0	$\Delta\nu_{\mathrm{MFS}}$	$\Delta\nu_S$	$\Delta\nu_r$	ν_{EFS}
$G_3 \rightarrow H_4$	A	14 765.04(3)						
			0.997(1)	14 726.22(2)	0.60(5)	0.02	0.00(1)	14 726.84(6)
	B	14 687.58(3)						
$G_4 \rightarrow H_5$	A	5 845.13(4)						
			0.966(2)	5 828.77(3)	0.14(5)	0.04	0.00(2)	5 828.95(6)
	B	5 812.47(4)						
$G_5 \rightarrow H_6$	A	10 056.91(10)						
			0.967(3)	10 031.54(6)	$-0.46(5)$	0.02	0.00(5)	10 031.10(9)
	B	10 006.27(6)						
$H_4 \rightarrow I_5$	A	5 678.80(8)						
			0.971(4)	5 663.02(5)	0.66(5)	0.01	0.00(2)	5 663.69(8)
	B	5 647.29(7)						
$H_5 \rightarrow I_6$	A	3 596.32(6)						
			0.947(7)	3 590.69(4)	$-0.02(5)$	0.00	0.00(7)	3 590.67(9)
	B	3 585.09(5)						
$H_6 \rightarrow I_7$	A	3 844.35(3)						
			0.952(3)	3 837.15(2)	$-0.35(5)$	0.02	0.00(5)	3 836.82(7)
	B	3 829.99(3)						
$I_7 \rightarrow K_8$	A	1 786.46(5)						
			0.968(8)	1 780.51(3)	$-0.04(5)$	0.00	0.00(1)	1 780.47(6)
	B	1 774.57(7)						

ν_0 was computed from Eq. (26).

The "pure EFS" interval is defined as the single interval at which transitions would be observed in the absence of magnetic fine structure. It has been estimated from the measured composite resonances by relying on calculations of the frequency offsets of the individual MFS components from the "pure EFS" interval. Since all the MFS operators except H_x have zero trace, an equivalent way of formally defining the "pure" EFS position for a particular EFS state is as the statistically weighted average position of the 12 MFS levels belonging to that state, corrected for the exchange energy,

$$E[(\nu,R)nL_N]$$
$$= \sum_{F,J_1,J} \frac{(2J+1)E[(\nu,R,F)nL_N(J_1,J)]}{\sum_{F,J_1,J}(2J+1)} + V_x/2 .$$

$$(30)$$

Since the four-peaked $\Delta N = 0$ resonances show partially resolved MFS, the extraction of the EFS interval from these resonances presents an opportunity to check the reliability of the MFS calculations. Using some assumed value for the relevant EFS interval, and calculated MFS energies for each state involved in the transition, a simulated line shape was prepared that consisted of a superpo-

sition of the 12 strongest transitions ($\Delta F = 0$, $\Delta J_1 = \Delta J = \Delta N = 0$) using Gaussian resonances whose positions relative to the EFS interval were taken from calculations of the MFS, and whose strengths were taken to be proportional to $2J + 1$. These simulations showed excellent qualitative agreement with the observed resonance shapes in all cases [30]. A more quantitative comparison can be obtained by fitting the simulated line shapes to the same four-Gaussian function used to fit the experimental data, and determining the offset $\Delta\nu_{\mathrm{MFS}}$ of the fitted position of each of the four component peaks from the assumed EFS interval. Subtracting these values from the fitted component peak positions in the experimental data leads to the four redundant determinations of the EFS interval for each transition that are shown in the last column of Table V. These results tend to agree with each other to within a few tenths of megahertz, but the scatter is somewhat larger than would be expected from statistical variation alone; the standard deviation expected from statistical errors of the fits are 0.18, 0.12, and 0.44 MHz for the $H_5 \rightarrow I_5$, $H_6 \rightarrow I_6$, and $I_7 \rightarrow K_7$ transitions, respectively, but the scatter of the sets of four independent measurements give 0.16, 0.24, and 0.87 MHz, respectively, for estimates of the standard deviation. The excess scatter in the four independent estimates of ν_{EFS} can be viewed as a test of the reliability of the calculated MFS. For instance, the four determinations of the $H_6 \rightarrow I_6$ EFS

interval, for which $\Delta\nu_{MFS}$ ranges from -54 to $+36$ MHz, give results consistent to within 0.24 MHz. Evidently the calculated MFS is reliable to better than 1% in this case. By a similar comparison of the scatter in the calculated MFS corrections to the scatter in the corrected results, in all three $\Delta N = 0$ cases, we conclude that the MFS is calculated to a precision of at least 2% in our model, and adopt this as an estimate of the reliability of the MFS corrections. At the same time, we recognize that the excess scatter in the sets of four results could be due to some other source of statistical variation, so we use the larger of the internal and external errors in assigning a statistical error to the mean result.

A systematic correction to these results comes from the Stark shifts in resonance frequencies due to the motional electric fields that were present within most of the microwave interaction regions. For the waveguide interaction regions, the earth's magnetic field was unshielded, leading to a motional electric field of about 0.3 V/cm. The small Stark shifts that result (all ≤ 0.1 MHz) were calculated and subtracted from the observed line positions. The coaxial region was magnetically shielded, and Stark shifts were considered negligible.

Another systematic effect that contributes to the apparent centers of the resonances is due to the reflected microwave traveling waves within the interaction regions, which were typically 0.3 by amplitude (Table IV). The resulting distortion of the resonance line shapes has been discussed elsewhere [27,28]. The resulting shift of the line center is given by

$$\Delta\nu^{refl} = \text{Re}(\Gamma)(1/4T)\frac{y\cos(\pi y)}{y^2 - \frac{1}{4}} \equiv \text{Re}(\Gamma)\Delta\nu^{max} , \qquad (31)$$

where $y \equiv 2\Delta\nu_D T$, with $\Delta\nu_D$ the Doppler shift, and T the geometrical transit time through the region. The shift is proportional to the real part of the reflection coefficient Γ, referred to the center of the region. If we regard the phase of Γ as unknown, then $|\Gamma|\Delta\nu^{max}$ sets a limit on the size of the expected shifts. To the extent that the reflection coefficients of the two (nominally identical) ends of the interaction region are equal, the shifts of the line centers would cancel in the average over the two directions of propagation. We assign an additional systematic error of $\Delta\nu_r = \pm 0.3|\Gamma|\Delta\nu^{max}$ to these intervals. In the one case where only one direction of propagation was studied, $I_7 \rightarrow K_7$, we assign an error of $\Delta\nu_r = \pm|\Gamma|\Delta\nu^{max}$.

Table V shows the mean results from the three $\Delta N = 0$ transitions, obtained from a straight average of results from each of the four peaks of the spectra, with a statistical error assigned as discussed above and also including uncertainty from the systematic errors. The most important of these is due to possible inaccuracies of the MFS model. Since the net contribution of the MFS correction to the mean value of each of these EFS intervals is ≤ 4 MHz, and we estimate that the correction is reliable to 2%, we assign an additional error of ± 0.1 MHz to each $\Delta N = 0$ interval.

Table VI shows the results from the measurements of $\Delta N = 1$ transitions. Most of the corrections and systematic errors for these transitions are similar to those discussed above; only the correction for MFS differs substantially. For these transitions the frequency offsets of the 12 individual MFS transitions is small, ranging over ± 4 MHz for the $G \rightarrow H$, ± 2 MHz for the $H \rightarrow I$, and ± 1 MHz for the $I \rightarrow K$ transitions. As a result, the primary uncertainty in $\Delta\nu_{MFS}$, the correction that accounts for the unresolved composite structure, is not due to the calculated positions of the component resonances (which are apparently correct to 2%), but rather to uncertainty in the relative strengths of the component resonances. Based on a careful comparison of the relative strengths of the four Gaussian fits of the simulated and observed $\Delta N = 0$ resonances, it appears that statistical weighting reproduces the relative peak strengths to within 10%. With this in mind, simulations of the $\Delta N = 1$ transitions were prepared consisting of 12 Gaussians whose positions are fixed at the calculated offset from an assumed EFS interval, and whose strengths are either (a) proportional to the statistical weight of the state of lesser J, or (b) as in (a) except additionally weighted by a linear function of frequency changing by 10% over the range of individual components. These simulations were fit to the same single Gaussian used to fit the data. The difference of the result found in (a) from the assumed EFS interval was taken as the best estimate of $\Delta\nu_{MFS}$ for each transition, and the uncertainty in this correction was taken to be the difference in the fitted centers found in (a) and (b), generally about 0.05 MHz. These corrections, and the "pure EFS" intervals that they imply, are shown in Table VI along with the other systematic corrections discussed above. In the case of the $G_5 \rightarrow H_6$ transition, good agreement is found with a previous determination based on measurements of somewhat better resolution [15].

IV. COMPARISON WITH THEORY

The measured EFS intervals may be compared with theory in several ways. The simplest way is to note that the ten measured intervals determine the relative positions of the 11 fine-structure levels shown in Fig. 2. Choosing the $(0,1)10K_8$ state as a reference level, and taking its energy (relative to zeroth order) to be -2731.90 MHz as predicted by the polarization model, the energies of the ten other levels are determined from experiment and are shown in the last column of Table VII. These can be compared directly with the predictions of the polarization model, and are found to give satisfactory agreement in all cases. The precision of this comparison, however, is limited by the rather large convergence errors assigned to the scalar constants A_0 in the polarization model.

A much more critical comparison between experiment and theory can be achieved by fitting the total energies, shown in the last column of Table VII, to obtain experimental estimates of the structure factors A_0 and A_2 for each L. The structure factor A_2 determines the relative positions of the three states of common L. The structure factor A_0 gives the statistically weighted average energy for the three states of common L, although due to the lack of an absolute energy determination, only differences

TABLE VII. Comparison of theoretical and experimental energies of 11 Rydberg levels measured in this study. The last column gives the total energy in MHz (relative to the zeroth-order Rydberg energy), as determined from experiment, with the energy of the K_8 state chosen to agree with theory. The other columns show the theoretically predicted contributions to each state's energy. One-standard-deviation errors are shown in parentheses.

State	A_0	$A_2\langle P_2 \rangle$	$E_{\mathrm{pol}}^{[2]}$	Theory total	E_{EFS}
G_3	$-8265(190)$	$-18\,157(6)$	$-429.8(36)$	$-26\,852(190)$	$-26\,785.39(26)$
G_4	$-8265(190)$	$25\,420(8)$	$-1\,003.6(41)$	$16\,151(190)$	$16\,252.50(21)$
G_5	$-8265(190)$	$-9244(3)$	$-947.3(21)$	$-18\,456(190)$	$-18\,380.27(13)$
H_4	$-2901(24)$	$-9056.2(70)$	$-111.24(15)$	$-12\,068(25)$	$-12\,058.55(25)$
H_5	$-2901(24)$	$13\,584.3(10)$	$-274.94(17)$	$10\,408(24)$	$10\,423.55(20)$
H_6	$-2901(24)$	$-5\,224.5(40)$	$-233.50(10)$	$-8\,359(24)$	$-8\,349.18(9)$
I_5	$-1194(4)$	$-5\,163.66(12)$	$-37.18(1)$	$-6\,394.8(40)$	$-6\,394.87(24)$
I_6	$-1194(4)$	$8\,114.50(19)$	$-90.03(1)$	$6\,830.5(40)$	$6\,832.88(18)$
I_7	$-1194(4)$	$-3\,245.80(7)$	$-72.31(1)$	$-4\,512.1(40)$	$-4\,512.36(6)$
K_7	$-548.9(10)$	$5\,235.87(4)$	-32.42	$4\,654.6(10)$	$4\,655.88(52)$
K_8	$-548.9(10)$	$-2\,155.87(2)$	-27.15	$-2\,731.9(10)$	$-2\,731.9$[a]

[a]The energy of the K_8 state is defined to be the theoretical value.

of scalar structure factors between states of different L can be determined from the data. The structure factors were determined in two ways. First, a least-square fit of the tabulated energies to the expression

$$E(L,N) = A_0(L) + A_2(L)\langle RLN | P_2(\cos\theta) RLN \rangle$$
$$+ E_{\mathrm{pol}}^{[2]}(L,N) \tag{32}$$

was found, where $E_{\mathrm{pol}}^{[2]}(L,N)$ is the calculated second-order polarization energy for each state, as defined in Eq. (12) and shown in Tables II and VII. The resulting least-squares-fit parameters are shown in the column of Table VIII labeled "two-parameter-fit." The errors in these parameters were conservatively computed by assuming that the contributing errors from the measured frequency in-

tervals were completely correlated. Similarly, the contributing errors from the calculated $E^{[2]}$ corrections were also assumed to be completely correlated. The parameter error was then computed from

$$(\delta A)^2 = \left[\sum_i \left| \frac{\partial A}{\partial v_i} \right| (\delta v_i) \right]^2 + \left[\sum_i \left| \frac{\partial A}{\partial E_i^{[2]}} \right| (\delta E_i^{[2]}) \right]^2 . \tag{33}$$

The quality of these "two-parameter" fits was only fair, reproducing the data with $\chi^2 = 14$ for three degrees of freedom.

As a second approach, the level positions were fit to a function of the form

TABLE VIII. Structure factors of the (0,1)10 Rydberg states of H$_2$. The second column lists the structure factors calculated from the higher-order polarization model (HOPM). The third column lists the structure factors obtained by fitting the state energies (Table VIII) and measured energy differences using a parametrization containing only $A_0(L)$ and $A_2(L)$ as parameters. If a third parameter $A_1(L)$ is added, as discussed in the text, the results are as shown in the last column. The units are MHz. The numbers in parenthesis are one-standard-deviation errors computed as described in the text.

Structure factors	HOPM	Two-parameter fit	Three-parameter fit
$A_0(G)$-$A_0(H)$	$-5\,364(189)$	$-5\,294.1(33)$	$-5\,293.9(33)$
$A_0(H)$-$A_0(I)$	$-1\,708(24)$	$-1\,696.0(5)$	$-1\,696.0(5)$
$A_0(I)$-$A_0(K)$	$-644.8(44)$	$-644.6(3)$	$-644.6(3)$
$A_2(G)$	$-127\,099(40)$	$-127\,197(16)$	$-127\,197(23)$
$A_2(H)$	$-67\,921.6(52)$	$-67\,938.4(9)$	$-67\,938.4(12)$
$A_2(I)$	$-40\,572.6(9)$	$-40\,580.5(5)$	$-40\,580.6(7)$
$A_2(K)$	$-26\,179.3(2)$	$-26\,183.6(18)$	$-26\,183.6(18)$
$A_1(G)$	0.0		$0.26(71)$
$A_1(H)$	0.0		$-0.073(49)$
$A_1(I)$	0.0		$-0.057(34)$

$$E(L,N) = A_0(L) + A_1(L)\langle RLN | \mathbf{R} \cdot \mathbf{L} | RLN \rangle$$

$$+ A_2(L)\langle RLN | P_2(\cos\theta) | RLN \rangle$$

$$+ E_{\text{pol}}^{[2]}(L,N) . \tag{34}$$

The parameter A_1 is predicted to be zero in the polarization model, but does represent another physically acceptable way to form a scalar quantity. In the case of the $10K$ states, where only two states are determined, A_1 was set equal to zero. This fit has just enough parameters to reproduce the data exactly. The indicated parameter values are shown in Table VIII, labeled "three-parameter fit." Again the parameter errors were computed from Eq. (33). A comparison of the results of the two fits shows that they yield essentially identical values of the A_0 and A_2 parameters, and that the parameters A_1 are close to zero. The results from the three-parameter fits are taken to represent the best experimental estimates of the structure factors A_0 and A_2. Also shown in Table VIII are the polarization-model predictions of these structure factors, from Table I. The experimentally determined scalar factors are in good agreement with these predictions and are considerably more precise. On the other hand, the tensor structure factors are systematically and significantly larger than the predictions. This confirms the behavior first reported after preliminary data analysis [16], but with some reduction of experimental uncertainty. One of the tensor structure factors, $A_2(G)$, has been determined previously from optical spectroscopy to be $-4.200(15)$ cm$^{-1} = -125\,913(450)$ MHz [10]. The 2.8σ discrepancy with the much more precise result of the present measurements suggests that systematic errors were underestimated in the optical spectroscopy.

We now consider what conclusions may be drawn about $H_2^+(0,1)$ electric properties from the observed Rydberg fine structure. The polarization model predicts the fine structure as a function of a small number of core properties, the most significant of which are the electric quadrupole moment (Q) and the scalar and tensor adiabatic dipole polarizabilities (α_S, α_T). As discussed above, the observed fine structure can be parametrized in terms of the scalar and tensor structure factors (A_0, A_2). This approach is convenient for displaying the L dependence of the structure, which is essential for separating the contributions from different terms in V_{pol}. Comparing the observed structure factors with predictions, it is possible to determine the values of core parameters Q, α_S, and α_T, which give the best fit to observations, effectively determining the core parameters experimentally [31]. These conclusions rest on the assumption that the *form* of the structure factors, Eqs. (35) and (41), is correctly predicted by the polarization model. As will be shown below, the present observations appear consistent with these expected forms, and complete agreement with experiment can be found by adjustment of Q, α_S, and α_T. However, it should be noted that should Eqs. (35) or (41) be found to be incomplete, conclusions regarding the core properties would require reexamination.

In the case of the scalar structure factors, the polariza-

tion model predicts that the results will be of the form

$$A_0(L) = B_4 \langle r^{-4} \rangle_L + B_6 \langle r^{-6} \rangle_L + T + E_{\text{rel}}(n,L) , \tag{35}$$

where T represents higher-order terms and E_{rel} is the leading relativistic correction to the Rydberg energy

$$E_{\text{rel}}(n,L) = \frac{\alpha^2 \text{Ryd}}{n^3} \left[-\frac{3}{4n} + \frac{1}{L + \frac{1}{2}} \right] , \tag{36}$$

which contributes approximately 4–7 MHz to the measured scalar constants, and the constants B_4 and B_6 are predicted, based on calculated core properties, to be

$$B_4^{\text{theor}} = -1.000\,544\frac{\alpha_S}{2} = -1.5913 \text{ a.u.}$$

and

$$B_6^{\text{theor}} = -\frac{C_0}{10} + \frac{3\beta_S}{2} = -2.41 + 10.26 = 7.85 \text{ a.u.}$$

T represents the possible effects of uncalculated terms proportional to r^{-7}, r^{-8}, etc. These are crudely estimated within the polarization model as

$$T \cong (-B_6\langle r^{-6}\rangle/2 \pm B_6\langle r^{-6}\rangle/2) . \tag{37}$$

Experimental observations are most clearly compared with these expectations by the use of a graphical construction. Correcting for E_{rel}, it is expected that

$$[A_0(L) - E_{\text{rel}}(n,L)] = B_4\langle r^{-4}\rangle_L + B_6\langle r^{-6}\rangle_L + T . \tag{38}$$

Subtracting the values of this expression for states of adjacent L, and dividing through by the differences of the expectation values $\langle r^{-4}\rangle$, this gives

$$\frac{\Delta(A_0 - E_{\text{rel}})}{\Delta\langle r^{-4}\rangle} = B_4 + B_6\frac{\Delta\langle r^{-6}\rangle}{\Delta\langle r^{-4}\rangle} + \frac{\Delta T}{\Delta\langle r^{-4}\rangle} . \tag{39}$$

When plotted as a function of the coefficient of B_6, this derived quantity should, except for the influence of higher terms, give a straight line with slope B_6 and intercept B_4. Such a plot is shown in Fig. 5, including the three points derived from the experimentally measured G-H, H-I, and I-K differences. The dashed line is the expectation based on calculated values of B_4 and B_6. The fact that the three points do not lie on a straight line indicates that higher terms are contributing significantly to the measured structure. However, their contribution appears substantially smaller than suggested by the polarization-model estimate discussed above, which would give the dashed-dotted line and an uncertainty given by the shaded area in Fig. 5. In order to extract the best experimental estimate of B_4 and B_6, the observed scalar constant differences are fit to the function

$$\Delta(A_0 - E_{\text{rel}}) = B_4\Delta\langle r^{-4}\rangle + B_6\Delta\langle r^{-6}\rangle + B_7\Delta\langle r^{-7}\rangle , \tag{40}$$

where the term proportional to r^{-7} is intended to account approximately for the contribution of higher terms. This fit gives

$$B_4^{\text{expt}} = -1.5894(17) \text{ a.u. },$$

$$B_6^{\text{expt}} = 8.4(8) \text{ a.u. },$$

and

$$B_7^{\text{expt}} = -21(6) \text{ a.u.}$$

The fitted values of B_4 and B_6 are both consistent with the predictions cited above. The fitted value of B_4 can be taken to give an experimental determination of the scalar dipole polarizability of $H_2^+(0,1)$ with the result

$$\langle \alpha_S \rangle_{0,1} = 3.1770(34)a_0^3 .$$

This is 0.1% lower than the calculated value [13], but is well within the range of uncertainty (0.3%) which we estimate results from the approximations made in those calculations regarding the effects of nuclear motion and neglect of nonadiabatic wave-function corrections. The fitted value of B_7 implies a contribution to $A_0(G)$ of $-122(35)$ MHz, which appears plausible, judging from the two terms of this order that have been calculated [10] and the fact that other terms, such as the nonadiabatic

quadrupole polarizability, which have not yet been calculated might be expected to be larger than these.

A similar examination of the tensor structure factors is somewhat more complex. In this case, it is expected that

$$A_2(L) = C_3 \langle r^{-3} \rangle + C_4 \langle r^{-4} \rangle + C_6 \langle r^{-6} \rangle + \mathcal{T} , \quad (41)$$

where the predicted values of C_3, C_4, and C_6 are

$$C_3^{\text{theor}} = -1.000\,172Q = -1.642\,90 \text{ a.u. },$$

$$C_4^{\text{theor}} = -1.000\,544\frac{\alpha}{3}T = -1.3432 \text{ a.u. },$$

and

$$C_6^{\text{theor}} = \frac{\beta_T}{2} - \frac{E_1}{7} - \frac{C_1}{7} = 6.24 - 3.82 - 0.73$$

$$= 1.69 \text{ a.u.}$$

When the observed values of $A_2(L)$ are divided by $\langle r^{-3} \rangle$ and plotted as a function of $\langle r^{-4} \rangle / \langle r^{-3} \rangle$, the result should, except for the C_6 and higher terms, be a straight line with intercept C_3 and slope C_4:

$$\frac{A_2(L)}{\langle r^{-3} \rangle} = C_3 + C_4 \frac{\langle r^{-4} \rangle}{\langle r^{-3} \rangle} + C_6 \frac{\langle r^{-6} \rangle}{\langle r^{-3} \rangle} + \frac{\mathcal{T}}{\langle r^{-3} \rangle} . \quad (42)$$

Such a plot of the experimental results is shown in Fig. 6. It clearly indicates a slope and intercept near the expect-
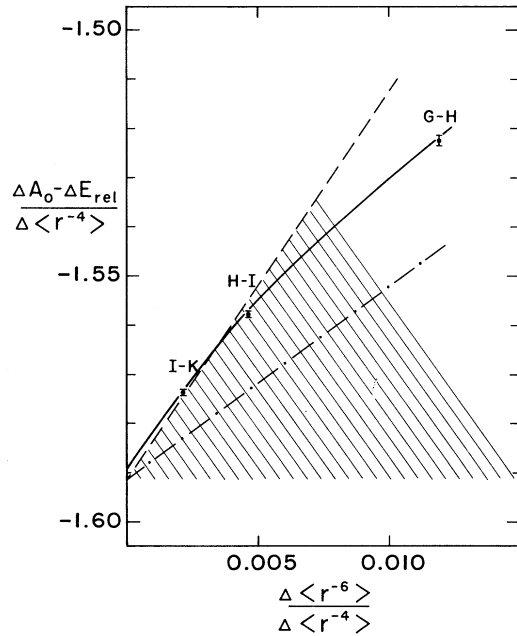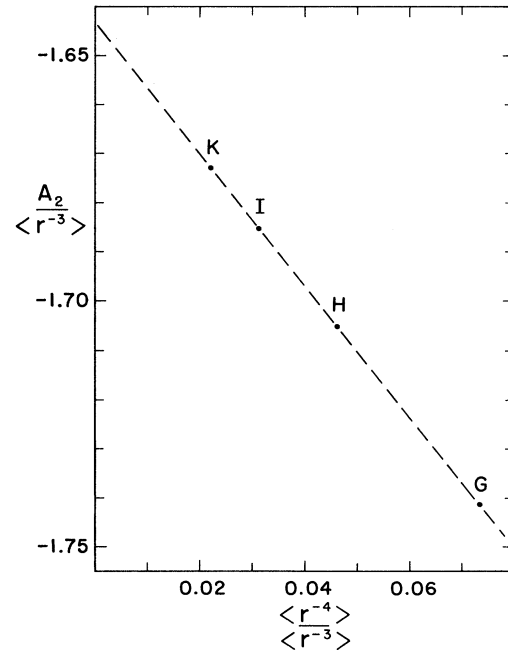

FIG. 5. Plot of scaled differences of measured Rydberg H_2 scalar structure constants (A_0), corrected for relativistic contributions. As described in the text, the intercept, slope, and curvature of this plot are associated with portions of the polarization potential proportional to r^{-s} with $s = 4$, 6, and ≥ 7, respectively. The dashed line shows the expected result, based on calculated H_2^+ properties and assuming that terms with $s \geq 7$ are negligible. The dashed-dotted line and the shaded area represent the results predicted by the polarization model, including an estimate of the $s \geq 7$ terms given by $(-\frac{1}{2} \pm \frac{1}{2})$ times the total $s = 6$ contribution. The solid curve is a fit of the data varying coefficients B_4, B_6, and B_7, as described in the text.

FIG. 6. Plot showing the variation of the measured Rydberg H_2 tensor structure factors (A_2) over a range of L. The plot is scaled so that its intercept and slope are related to the portions of the polarization potential proportional to r^{-3} and r^{-4}, respectively, if higher-order contributions are negligible. Measurement errors are smaller than the plotted points.

ed values. Before drawing any conclusions, however, the possible influence of the C_6 and higher terms needs to be carefully considered. In order to examine this, it is helpful to examine the *slope* of the curve plotted in Fig. 6. This is accomplished by taking differences of the ratio $A_2/\langle r^{-3}\rangle$ between states of adjacent L, and then dividing through by the difference of the ratio $\langle r^{-4}\rangle/\langle r^{-3}\rangle$ to form the derived quantity

$$\frac{\Delta(A_2/\langle r^{-3}\rangle)}{\Delta(\langle r^{-4}\rangle/\langle r^{-3}\rangle)}=C_4+C_6\frac{\Delta(\langle r^{-6}\rangle/\langle r^{-3}\rangle)}{\Delta(\langle r^{-4}\rangle/\langle r^{-3}\rangle)}$$
$$+\frac{\Delta[T/\langle r^{-3}\rangle]}{\Delta(\langle r^{-4}\rangle/\langle r^{-3}\rangle)}. \quad (43)$$

When plotted as a function of the coefficient of C_6, this quantity should, except for the influence of the higher terms, give a straight line with intercept C_4 and slope C_6, which is somewhat analogous to the plot in Fig. 5. Such a plot is shown in Fig. 7, where, as in Fig. 5, the expected values in the absence of higher terms are shown by the dashed line, and the polarization-model estimate of the higher-term contribution is shown by the dashed-dotted curve and the shaded area. In contrast to Fig. 5, the
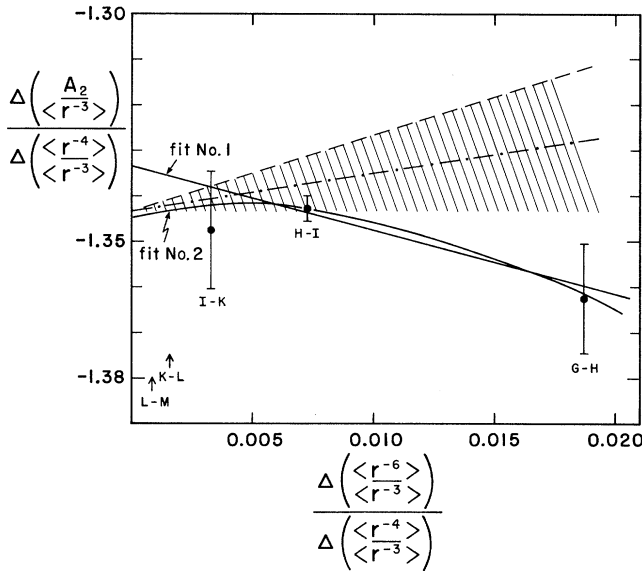

FIG. 7. Plot showing the variation in slope of the plot of Fig. 6 over the range of L studied. As in Fig. 5, the intercept, slope, and curvature of the quantity plotted here are associated with portions of the polarization potential proportional to r^{-s} with $s=4$, 6, and ≥ 7, respectively. The dashed line is again the expected behavior based on calculated H_2^+ properties if the $s\geq 7$ terms are negligible, and the dashed-dotted curve and shaded area show the region consistent with polarization-model estimates of the $s\geq 7$ contributions. The two solid curves represent alternative extrapolations of the data, described in the text. The approximately 1% difference in the extrapolated intercepts limits the precision with which the tensor polarizability α_T can be inferred from the data, which in turn limits the precision of the determination of the quadrupole moment Q.

three points in Fig. 7 are consistent with a straight line. However, the slope of that line, -1.4 ± 1.0, is very different from the calculated value of C_6 ($+1.69$). Perhaps this indicates that the calculated value of C_6 is incorrect. However, an alternative explanation is that the higher terms are contributing at a level somewhat larger than that predicted by the polarization-model estimate. Since the data cannot discriminate between these two possible interpretations, we consider the implications of each for the best estimates of C_3 and C_4. In the first case, allowing for the fact that C_6 may be in error, the data are fit to the function

$$A_2(L)=C_3\langle r^{-3}\rangle+C_4\langle r^{-4}\rangle+C_6\langle r^{-6}\rangle. \quad (44)$$

This gives a good fit, $\chi^2=0.59$ for one degree of freedom, and the least-square parameters

$$C_3^{\text{expt1}}=-1.643\,35(22) \text{ a.u. },$$

$$C_4^{\text{expt1}}=-1.3336(81) \text{ a.u. },$$

$$C_6^{\text{expt}}=-1.4(10) \text{ a.u.}$$

In the second case, if the higher terms are the most significant factor, C_6 is fixed at its calculated value and the data are fit to the function

$$A_2(L)=C_3\langle r^{-3}\rangle+C_4\langle r^{-4}\rangle+1.69\langle r^{-6}\rangle+C_7\langle r^{-7}\rangle,$$
$$\quad (45)$$

where again the term proportional to r^{-7} is intended to approximate the effect of the higher terms. This also gives a good fit, $\chi^2=0.16$ for one degree of freedom, and gives the least-square parameters

$$C_3^{\text{expt2}}=-1.643\,11(15) \text{ a.u. },$$

$$C_4^{\text{expt2}}=-1.3447(47) \text{ a.u. },$$

$$C_7^{\text{expt}}=-18.5(5.9) \text{ a.u.}$$

The fitted value of C_7 implies a contribution to $A_2(G)$ of $-109(35)$ MHz, in contrast to the polarization-model estimate of -40 ± 40 MHz. Both of these fits are illustrated in Fig. 7, labeled fits 1 and 2, respectively. Their different intercepts imply different slopes of the curve of Fig. 6 near the origin, with consequent changes in both C_3 and C_4. Figure 8 further illustrates the implications of the choice of fitting procedure by plotting the limits of confidence in the parameters C_3 and C_4 from the two fits. These curves are taken to be the projections of the elipsoidal surface of $\chi^2=2.0$ into the C_3-C_4 plane. Clearly the results are quite sensitive to the interpretation of Fig. 7 and the choice of fit. Since either interpretation is consistent with the data, the best experimental estimates of the parameters C_3 and C_4 are taken to be the average of the results of the two fits, with error bars expanded to include the one-standard-deviation limits of both fits. This gives

$$C_3^{\text{expt}}=-1.643\,23(30) \text{ a.u. },$$

$$C_4^{\text{expt}}=-1.339(12) \text{ a.u. },$$

TABLE IX. Selection rules for the MFS operators, shown in Eqs. (17)–(19), between $(v,R,F)nL_N(J_1,J)$ basis states. All the operators obey the selection rules $\Delta J = \Delta I = 0$. Additional selection rules are shown in the table. The quantum numbers are defined in the text. Matrix elements off diagonal in L and R are numerically insignificant in determining the second-order magnetic-fine-structure energies for $n = 10$ states.

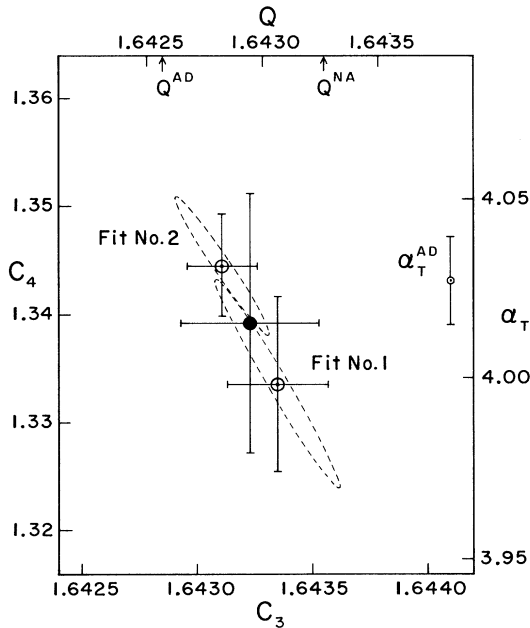| Term	ΔJ_1	ΔN	ΔF	ΔL	ΔR
$\mathbf{I}\cdot\mathbf{S}_1$	0	0	0	0	0
$\mathbf{T}^{[2]}\cdot\mathbf{T}^{[2]}$	0	$0,\pm1,\pm2$	$0,\pm1$	0	$0,\pm2$
$\mathbf{S}_1\cdot\mathbf{R}$	0	$0,\pm1$	$0,\pm1$	0	0
$\mathbf{L}\cdot\mathbf{S}_2$	$0,\pm1$	$0,\pm1$	0	0	0
$\mathbf{L}\cdot\mathbf{S}_1$	0	$0,\pm1$	$0,\pm1$	0	0
$\mathbf{S}_2\cdot[\mathbf{S}_1-3\hat{\mathbf{r}}(\mathbf{S}_1\cdot\hat{\mathbf{r}})]$	$0,\pm1$	$0,\pm1,\pm2$	$0,\pm1$	$0,\pm2$	0
$0.5+2(\mathbf{S}_1\cdot\mathbf{S}_2)$	$0,\pm1$	0	$0,\pm1$	0	0

FIG. 8. Plot illustrating the limits on the fitted coefficients C_3 and C_4 imposed by the measured tensor structure factors (A_2). The left vertical axis measures C_4 (in a.u.), while the right vertical axis measures the equivalent parameter $\alpha_T(a_0^3)$. The bottom horizontal axis measures C_3 (in a.u.), while the top horizontal axis plots the equivalent parameter Q (ea_0^2). The ellipses and open circles show the results of two different fitting procedures described in the text. The ellipses are the projections of the surface of $\chi^2 = 2.0$ into the C_3–C_4 plane, and the error bars on the open circles are standard errors from the fits. The solid point shows the average of the results from the two fitting procedures, which is taken to be the best experimental estimate of C_3 and C_4. For comparison, the best calculated value of α_T is shown at the right, with 0.3% error bars to reflect the approximations made in the calculations. At the top are shown two calculated results for the quadrupole moment Q. The result from the nonadiabatic calculation Q^{NA} is expected to be most reliable. The data indicate that the calculated values of α_T and Q^{NA} cannot both be correct.

which imply the following values of the H$_2^+$ electrical properties:

$$\langle Q \rangle_{0,1} = 1.642\,95(30)ea_0^2 \ ,$$

$$\langle \alpha_T \rangle_{0,1} = 4.015(36)a_0^3 \ .$$

Since Q and α_T are linearly related to C_3 and C_4, these alternate labels for the axes of Fig. 8 are also shown there.

The result for α_T is consistent with the theoretical prediction [13]

$$\alpha_T^{\text{theor}} = 4.0273 \pm 0.3\% \ ,$$

where the estimate of error is our guess of the possible effects of the nuclear motion and adiabatic wave-function approximations. The experimental result for Q lies approximately midway between the adiabatic prediction [13]

$$\langle Q \rangle_{0,1}^{\text{AD}} = 1.642\,57ea_0^2$$

and the more recent, and presumably more reliable, result of calculations employing the full nonadiabatic wave function [32,19]

$$\langle Q \rangle_{0,1}^{\text{NA}} = 1.643\,27ea_0^2 \ ,$$

and is consistent with either result.

It is important to note, however, that the possible values of Q and α_T that are consistent with the data are highly correlated, as illustrated in Fig. 8. In particular, the calculated nonadiabatic value of Q and the calculated value of α_T, taken together, are in poor agreement with the data. If α_T is correct to within the 0.3% error estimate (as we *assumed* in our preliminary report), then a value of Q of about 1.642 85(15) is indicated by the data. This result is in disagreement (2.2σ) with the results of the recent nonadiabatic calculations. On the other hand, if Q^{NA} is correct, then a value of α_T more than 1% below the calculation is required. Each of these scenarios also favors one or the other interpretations of Fig. 7. With some oversimplification, it appears that either (a) C_6^{theor} is correct, α_T^{theor} is correct, and Q^{NA} is wrong, or (b) C_6^{theor}

is wrong, α_T^{theor} is wrong, and Q^{NA} is correct are allowed by the present data. Based on the brief discussion of Ref. [19], it appears unlikely that relativistic corrections to the quadrupole moment, estimated there as $\cong -0.000\,08ea_0^2$, can account for the discrepancy in the first case.

The measurements reported here do not by any means represent the ultimate precision with which these Rydberg fine structures can be measured. Analogous fine-structure intervals in Rydberg states of the helium atom

have been measured by us with precision of approximately ± 0.01 MHz [28], and there is no fundamental reason why similar precision should not be possible in H_2 also. Future experimental measurements of improved precision should clarify the ambiguities left by the present results, and should lead to improved determinations of the H_2^+ properties Q, α_S, and α_T. The simplest improvement would be more precise measurement of the $n = 10$ $I \rightarrow K$ intervals. Other helpful new measurements would be

TABLE X. Contributions to the MFS energy for all of the $(0,1)10H$ states. The states are labeled $(F)L_N(J_1,J)$. The ratio of the diagonal matrix element of H_x [Eq. (19)] to the exchange energy V_x is listed in the second column. The third column shows the first-order MFS energy due to H_{hyp} [Eq. (17)], except that the magnetic dipole hyperfine structure $(b+c/3)\mathbf{I}\cdot\mathbf{S}_1$ is omitted. The first-order MFS due to H_{mag} [Eq. (19)] follows. The total second-order MFS energy is shown in the fifth column, and the total MFS contribution to the state energy is listed in the last column. All units are MHz.

State	H_x/V_x	$E_{\text{hyp}}^{[1]}$	$E_{\text{mag}}^{[1]}$	$E_{\text{MFS}}^{[2]}$	$E_{\text{MFS}}^{\text{tot}}$
$(\frac{1}{2})H_4(3.5,3.0)$	-0.33	-7.07	-5.54	-0.23	-12.85
$(\frac{1}{2})H_4(3.5,4.0)$	-0.63	-7.07	0.54	-0.23	-6.76
$(\frac{1}{2})H_4(4.5,4.0)$	-0.70	5.65	-1.27	-0.70	3.68
$(\frac{1}{2})H_4(4.5,5.0)$	-0.33	5.65	4.13	-0.68	9.10
$(\frac{3}{2})H_4(2.5,2.0)$	-1.00	12.64	3.89	0.00	16.53
$(\frac{3}{2})H_4(2.5,3.0)$	-0.14	12.64	8.14	0.31	21.60
$(\frac{3}{2})H_4(3.5,3.0)$	-0.52	14.73	0.94	-0.10	15.57
$(\frac{3}{2})H_4(3.5,4.0)$	-0.48	14.73	5.31	0.32	20.36
$(\frac{3}{2})H_4(4.5,4.0)$	-0.19	6.22	-3.22	0.26	3.26
$(\frac{3}{2})H_4(4.5,5.0)$	-0.76	6.22	1.86	0.40	8.48
$(\frac{3}{2})H_4(5.5,5.0)$	0.09	-21.32	-8.53	-0.59	-30.44
$(\frac{3}{2})H_4(5.5,6.0)$	-1.00	-21.32	-2.19	-0.54	-24.05
$(\frac{1}{2})H_5(4.5,4.0)$	-0.33	1.41	-5.34	-0.10	-4.03
$(\frac{1}{2})H_5(4.5,5.0)$	-0.64	1.41	0.64	-0.05	2.00
$(\frac{1}{2})H_5(5.5,5.0)$	-0.70	-1.18	-1.18	-0.03	-2.39
$(\frac{1}{2})H_5(5.5,6.0)$	-0.33	-1.18	4.15	-0.01	2.96
$(\frac{3}{2})H_5(3.5,3.0)$	-1.00	18.02	3.72	0.02	21.76
$(\frac{3}{2})H_5(3.5,4.0)$	-0.11	18.02	8.06	0.05	26.13
$(\frac{3}{2})H_5(4.5,4.0)$	-0.55	-13.25	0.56	0.28	-12.41
$(\frac{3}{2})H_5(4.5,5.0)$	-0.45	-13.25	5.14	0.39	-7.72
$(\frac{3}{2})H_5(5.5,5.0)$	-0.21	-20.08	-3.53	0.06	-23.52
$(\frac{3}{2})H_5(5.5,6.0)$	-0.74	20.08	1.72	0.15	-18.21
$(\frac{3}{2})H_5(6.5,6.0)$	0.08	16.38	-8.51	0.06	7.93
$(\frac{3}{2})H_5(6.5,7.0)$	-1.00	16.38	-2.20	0.01	14.19
$(\frac{1}{2})H_6(5.5,5.0)$	-0.33	8.24	-5.38	-0.28	2.58
$(\frac{1}{2})H_6(5.5,6.0)$	-0.64	8.24	0.74	-0.31	8.67
$(\frac{1}{2})H_6(6.5,6.0)$	-0.69	-7.07	-1.14	-0.07	-8.28
$(\frac{1}{2})H_6(6.5,7.0)$	-0.33	-7.07	4.29	-0.09	-2.87
$(\frac{3}{2})H_6(4.5,4.0)$	-1.00	-38.35	3.75	0.12	-34.48
$(\frac{3}{2})H_6(4.5,5.0)$	-0.09	-38.35	8.19	0.08	-30.08
$(\frac{3}{2})H_6(5.5,5.0)$	-0.58	-3.99	-5.55	0.67	-8.87
$(\frac{3}{2})H_6(5.5,6.0)$	-0.44	-3.99	5.15	0.54	1.70
$(\frac{3}{2})H_6(6.5,6.0)$	-0.23	16.38	-3.83	0.18	12.73
$(\frac{3}{2})H_6(6.5,7.0)$	-0.73	16.38	1.67	0.16	18.21
$(\frac{3}{2})H_6(7.5,7.0)$	0.07	12.64	-8.78	-0.08	3.94
$(\frac{3}{2})H_6(7.5,8.0)$	-1.00	12.64	-2.25	0.00	10.39

higher precision measurements at the highest possible L. For instance, the $n=10$, $L=7-9$ intervals would appear as indicated in Fig. 7, and could be of great assistance in determining the intercept of that curve, which is the critical question in interpreting the results. Since the contributions of terms proportional to r^{-7} and r^{-8} are important in the data analysis, it would be very helpful if the polarization model could be consistently extended to include all terms of this order, as has been done in the helium atom. This would greatly facilitate the use of that model to infer H$_2^+$ properties from the experimental results.

In summary, the fine structure of $(0,1)10L_N$ Rydberg states of H$_2$, with $4 \leq L \leq 7$, has been mapped experimentally with six-digit precision. The results are found to be completely consistent with the predictions of the polarization model if allowance is made for adjustment of the three leading parameters that characterize the long-range electric properties of the free H$_2^+$ ion, the quadrupole moment, and the scalar and tensor dipole polarizabilities. This adjustment yields experimental determinations of these three quantities, which are found to be largely, but not totally, consistent with existing calculations.

ACKNOWLEDGMENTS

APPENDIX

This appendix explicitly lists the formulas for the matrix elements contained in Eqs. (16)–(19). The angular momenta are defined in the text, and the basis states are coupled as follows:

$$|\psi\rangle = |[(\mathbf{R},L;\mathbf{N}),(\mathbf{I},\mathbf{S}_1;\mathbf{F});\mathbf{J}_1],\mathbf{S}_2;\mathbf{J}\rangle \ . \tag{A1}$$

In what follows the sign conventions are the same as those used by Edmonds [33].

The first two terms of Eq. (17) can be rewritten [32] as

$$b(\mathbf{I}\cdot\mathbf{S}_1)+c(\mathbf{I}\cdot\hat{\rho})(\hat{\rho}\cdot\mathbf{S}_1)=[b+(c/3)](\mathbf{I}\cdot\mathbf{S}_1)$$
$$+c\mathbf{T}^{[2]}(\mathbf{I},\mathbf{S}_1)\cdot\mathbf{T}^{[2]}(\hat{\rho},\hat{\rho}) \ , \tag{A2}$$

where $\mathbf{T}^{[2]}(\mathbf{r},\mathbf{s})$ denotes the second-rank irreducible tensor operator which is the tensor product of vector operators $\mathbf{r}$ and $\mathbf{s}$. One can then rewrite Eq. (17) as

$$H_{\text{hyp}}=[b+(c/3)](\mathbf{I}\cdot\mathbf{S}_1)+c\mathbf{T}^{[2]}(\mathbf{I},\mathbf{S}_1)\cdot\mathbf{T}^{[2]}(\hat{\rho},\hat{\rho})$$
$$+d(\mathbf{R}\cdot\mathbf{S}_1) \ . \tag{A3}$$

Of the various terms in H^{MFS}, only the $\mathbf{I}\cdot\mathbf{S}_1$ term is completely diagonal in the chosen basis. It contributes an energy of $+0.5[b+(c/3)]$ to the $F=\frac{3}{2}$ states and $-[b+(c/3)]$ to the $F=\frac{1}{2}$ states. Since the allowed electric dipole transitions between the $(v,R,F)nL_N$ states obey the selection rule $\Delta F=0$, this energy does not contribute directly to the observed transition frequencies, and can be considered part of the core energy. We note, however, that this term will contribute to the observed transition frequencies indirectly through the effects of mixing of different basis states.

In the following,

$$\begin{bmatrix} a_1 & a_2 & a_3 \\ a_4 & a_5 & a_6 \end{bmatrix}, \quad \begin{Bmatrix} a_1 & a_2 & a_3 \\ a_4 & a_5 & a_6 \end{Bmatrix},$$

and

$$\begin{Bmatrix} a_1 & a_2 & a_3 \\ a_4 & a_5 & a_6 \\ a_7 & a_8 & a_9 \end{Bmatrix}$$

are Wigner 3-J, 6-J, and 9-J symbols, respectively [33]. The matrix elements follow:

$$\langle\psi'|\mathbf{I}\cdot\mathbf{S}_1|\psi\rangle = \frac{F(F+1)-I(I+1)-S_1(S_1+1)}{2} \ , \tag{A4}$$

$$\langle\psi'|\mathbf{T}^{[2]}(\mathbf{I},\mathbf{S}_1)\cdot\mathbf{T}^{[2]}(\hat{\rho},\hat{\rho})|\psi\rangle = (-1)^{J_1+F'+L}[5I(I+1)(2I+1)(2F+1)(2F'+1)(2R+1)(2R'+1)(2N+1)(2N'+1)]^{1/2}$$
$$\times \begin{bmatrix} R' & 2 & R \\ 0 & 0 & 0 \end{bmatrix} \begin{Bmatrix} J_1 & N' & F' \\ 2 & F & N \end{Bmatrix} \begin{Bmatrix} L & R' & N' \\ 2 & N & R \end{Bmatrix} \begin{Bmatrix} S_1 & S_1 & 1 \\ I & I & 1 \\ F' & F & 2 \end{Bmatrix} \ , \tag{A5}$$

$$\langle\psi'|\mathbf{R}\cdot\mathbf{S}_1|\psi\rangle = (-1)^{J_1+2F'+R+L+I+3/2}[\tfrac{3}{2}R(R+1)(2R+1)(2F+1)(2F'+1)(2N+1)(2N'+1)]^{1/2}$$
$$\times \begin{Bmatrix} J_1 & N' & F' \\ 1 & F & N \end{Bmatrix} \begin{Bmatrix} I & S_1 & F' \\ 1 & F & S_1 \end{Bmatrix} \begin{Bmatrix} L & R & N' \\ 1 & N & R \end{Bmatrix} \ , \tag{A6}$$

$$\langle \psi'|\mathbf{L}\cdot\mathbf{S}_2|\psi\rangle =(-1)^{J+2J_1+F+R+L+1/2}[\tfrac{3}{2}L(L+1)(2L+1)(2N+1)(2N'+1)(2J_1+1)(2J_1'+1)]^{1/2}$$

$$\times \begin{Bmatrix} J & S_2 & J_1' \\ 1 & J_1 & S_2 \end{Bmatrix} \begin{Bmatrix} F & N' & J_1' \\ 1 & J_1 & N \end{Bmatrix} \begin{Bmatrix} R & L & N' \\ 1 & N & L \end{Bmatrix}, \tag{A7}$$

$$\langle \psi'|\mathbf{L}\cdot\mathbf{S}_1|\psi\rangle =(-1)^{J_1+2F'+N+N'+R+L+I+1/2}$$

$$\times [\tfrac{3}{2}L(L+1)(2L+1)(2N+1)(2N'+1)(2F+1)(2F'+1)]^{1/2}$$

$$\times \begin{Bmatrix} J_1 & F' & N' \\ 1 & N & F \end{Bmatrix} \begin{Bmatrix} R & L & N' \\ 1 & N & L \end{Bmatrix} \begin{Bmatrix} I & S_1 & F' \\ 1 & F & S_1 \end{Bmatrix}, \tag{A8}$$

$$\langle \psi'|\mathbf{S}_1\cdot\mathbf{S}_2|\psi\rangle =(-1)^{J+N+J_1'+J_1+F+F'+I+1}\tfrac{3}{2}[(2J_1+1)(2J_1'+1)(2F+1)(2F'+1)]^{1/2}$$

$$\times \begin{Bmatrix} J & S_2 & J_1' \\ 1 & J_1 & S_2 \end{Bmatrix} \begin{Bmatrix} N & F' & J_1' \\ 1 & J_1 & F \end{Bmatrix} \begin{Bmatrix} I & S_1 & F' \\ 1 & F & S_1 \end{Bmatrix}, \tag{A9}$$

$$\langle \psi'|\mathbf{S}_2\cdot[\mathbf{S}_1-3\hat{\mathbf{r}}(\hat{\mathbf{r}}\cdot\mathbf{S}_1)]|\psi\rangle =(-1)^{J+J_1+N'+F'+R+L+L'+I}$$

$$\times \tfrac{3}{2}[30(2J_1+1)(2J_1'+1)(2F+1)(2F'+1)(2N+1)(2N'+1)(2L+1)(2L'+1)]^{1/2}$$

$$\times \begin{pmatrix} L' & 2 & L \\ 0 & 0 & 0 \end{pmatrix} \begin{Bmatrix} J & S_2 & J_1' \\ 1 & J_1 & S_2 \end{Bmatrix} \begin{Bmatrix} I & S_1 & F' \\ 1 & F & S_1 \end{Bmatrix} \begin{Bmatrix} R & L' & N' \\ 2 & N & L \end{Bmatrix} \begin{Bmatrix} F' & F & 1 \\ N' & N & 2 \\ J_1' & J_1 & 1 \end{Bmatrix}. \tag{A10}$$

The selection rules between the various quantum numbers for each of the above terms are listed in Table IX. In order to demonstrate the size of the terms involved, we explicitly list in Table X the contribution of Eqs. (16)–(19) and (21) to the energy of the $(0,1,F)10H_N(J_1,J)$ states.

The relative intensities S of individual MFS transitions within a family of EFS transitions may be estimated as [33]

$$S(\psi',\psi)=\sum_m |\langle \psi'|z|\psi\rangle|^2=|\langle \psi||\mathbf{r}||\psi\rangle|^2/3, \tag{A11}$$

where the last term is the square of a reduced matrix element, which is given by

$$\langle \psi'||\mathbf{r}||\psi\rangle =(-1)^{J+J_1+J_1'+F+R+L+L'+3/2}[(2J+1)(2J'+1)(2J_1+1)(2J_1'+1)(2N+1)(2N'+1)(2L+1)(2L'+1)]^{1/2}$$

$$\times \begin{pmatrix} L' & 1 & L \\ 0 & 0 & 0 \end{pmatrix} \begin{Bmatrix} S_2 & J_1' & J' \\ 1 & J & J_1 \end{Bmatrix} \begin{Bmatrix} F & N' & J_1' \\ 1 & J_1 & N \end{Bmatrix} \begin{Bmatrix} R & L' & N' \\ 1 & N & L \end{Bmatrix} \frac{3n}{2}(n^2-L_>^2)^{1/2}, \tag{A12}$$

where $L_>$ is the greater of (L,L').

---

*Present address: Department of Physics and Astronomy, Youngstown State University, Youngstown, OH 44555.

†Present address: Department of Physics, Occidental College, Los Angeles, CA 90041.

[1] For a review, see Alan Carrington, Iain R. Mcnab, and Christine A. Montgomerie, J. Phys. B 22, 3551 (1989).

[2] K. B. Jefferts, Phys. Rev. Lett. 20, 39 (1968); 23, 1476 (1969).

[3] J. F. Babb and A. Dalgarno, Phys. Rev. Lett. 66, 880 (1991).

[4] William H. Wing, George A. Ruff, Willis E. Lamb, Jr., and Joseph J. Spezeski, Phys. Rev. Lett. 36, 1488 (1976).

[5] See, for example, Alan Carrington, Iain R. Mcnab, and Christine A. Montgomerie, Mol. Phys. 64, 983 (1988), and included references.

[6] L. Wolniewicz and J. D. Poll, Mol. Phys. 59, 953 (1986).

[7] G. G. Balint-Kurti, R. E. Moss, I. A. Sadler, and M. Shapiro, Phys. Rev. A 41, 4913 (1990).

[8] R. Loch, R. Stengler, and G. Werth, Phys. Rev. A 38, 5484 (1988).

[9] R. A. Hegstrom, Phys. Rev. A 19, 17 (1979).

[10] W. G. Sturrus, E. A. Hessels, P. W. Arcuni, and S. R. Lundeen, Phys. Rev. A 38, 135 (1988).

[11] P. W. Arcuni, E. A. Hessels, and S. R. Lundeen, Phys. Rev. A 41, 3648 (1990).

[12] Richard J. Drachman, Phys. Rev. A 26, 1228 (1982); 31, 1253 (1985).

[13] David M. Bishop and B. Lam, Mol. Phys. 65, 679 (1988).

[14] G. W. F. Drake, Phys. Rev. Lett. 65, 679 (1990).

[15] W. G. Sturrus, E. A. Hessels, and S. R. Lundeen, Phys. Rev. Lett. 57, 1863 (1986).

[16] W. G. Sturrus, E. A. Hessels, P. W. Arcuni, and S. R. Lundeen, Phys. Rev. Lett. 61, 2320 (1988).

[17] Richard J. Drachman, Phys. Rev. A 33, 2780 (1986).

[18] Richard J. Drachman, Phys. Rev. A 37, 979 (1988).

[19] David M. Bishop, Phys. Rev. Lett. 62, 3008 (1989).

[20] S. A. Blundell and S. R. Lundeen (unpublished).

[21] David M. Bishop, L. M. Cheung, and A. D. Buckingham, Mol. Phys. **41**, 1225 (1980); J. M. Shulman, R. Detrano, and J. I. Musher, Phys. Rev. A **5**, 1125 (1972).

[22] David M. Bishop (private communication); see also David M. Bishop and Lap M. Cheung, J. Phys. B **11**, 3133 (1978).

[23] K. Bockasten, Phys. Rev. A **9**, 1087 (1974).

[24] David M. Bishop (private communication).

[25] R. P. McEachran, C. J. Veenstra, and M. Cohen, Chem. Phys. Lett. **59**, 275 (1978).

[26] W. G. Sturrus, P. E. Sobol, and S. R. Lundeen, Phys. Rev. Lett. **54**, 792 (1985).

[27] E. A. Hessels, W. G. Sturrus, and S. R. Lundeen, Phys. Rev. A **38**, 4574 (1988).

[28] E. A. Hessels, F. J. Deck, P. W. Arcuni, and S. R. Lundeen, Phys. Rev. A **41**, 3663 (1990).

[29] K. A. Safinya, Ph.D. thesis, Harvard University, 1979.

[30] W. G. Sturrus, Ph.D. thesis, University of Notre Dame, 1988.

[31] A possible objection to this procedure is that the *theoretical* values of core parameters are used in calculating the second-order polarization energies (see Table VII), which are used to extract the structure factors from the observations, so the structure factors are not, in fact, obtained wholely from experiment. However, the dependence of the second-order energies on the parameter values is sufficiently weak, and the values determined from experiment are sufficiently close to the theoretical values that equivalent results would be obtained from a more complex self-consistent procedure on which reliance on the calculated values of Q, α_S, and α_T is eliminated.

[32] R. E. Moss, Chem. Phys. Lett. **172**, 458 (1990).

[33] A. R. Edmonds, *Angular Momentum in Quantum Mechanics* (Princeton University, Princeton, NJ, 1960).